AGU100 ADVANCING EARTH AND SPACE SCIENCE

Water Resources Research

RESEARCH ARTICLE
10.1029/2018WR023172

**Key Points:**
- We derive new regime-specific upscaled equations based on an analogy with two-phase flow in a capillary tube
- We demonstrate that the impact of pore-scale flow regimes on relative permeabilities is significant
- We discuss the limitations and the applicability of both the proposed upscaled equations and the classical two-phase Darcy's law

**Correspondence to:**
I. Battiato,
ibattiat@stanford.edu

**Citation:**
Picchi, D., & Battiato, I. (2018). The impact of pore-scale flow regimes on upscaling of immiscible two-phase flow in porous media. *Water Resources Research*, *54*. https://doi.org/10.1029/2018WR023172

Received 19 APR 2018
Accepted 1 AUG 2018
Accepted article online 13 AUG 2018



# The Impact of Pore-Scale Flow Regimes on Upscaling of Immiscible Two-Phase Flow in Porous Media

**D. Picchi**[1] **and I. Battiato**[1]

[1]Department of Energy Resources Engineering, Stanford University, CA, USA

**Abstract** Empirical or theoretical extensions of Darcy's law for immiscible two-phase flow have shown significant limitations in properly modeling the flow at the continuum scale. We tackle this problem by proposing a set of upscaled equations based on pore-scale flow regimes, that is, the topology of flowing phases. The incompressible Navier-Stokes equation is upscaled by means of multiple-scale expansions and its closures derived from the mechanical energy balance for different flow regimes at the pore scale. We also derive the applicability conditions of the upscaled equations based on the order of magnitude of relevant dimensionless numbers, that is, Eotvos, Reynolds, capillary, Froude numbers, and the viscosity and density ratio of the system, as well as a set of closures valid for the basic flow regimes of low Eotvos number systems, that is, core-annular and plug and drop traffic flows. We provide analytical expressions for the relative permeability of the wetting and nonwetting phases in different flow regimes and demonstrate that the effect of the flowing-phases topology on the relative permeabilities is significant. Finally, we show that the classical two-phase Darcy law is recovered for a limited range of operative conditions, while specific terms accounting for interfacial and wall interactions should be incorporated to accurately model ganglia or drop traffic flow.

## 1. Introduction

The flow of two immiscible fluids through porous media is frequently encountered in many engineering applications, such as enhanced oil recovery (Lake, 1989), carbon sequestration (Yang et al., 2008), wetting and drying processes (Lenormand et al., 1983), environmental contaminants transport in aquifers (Bear & Cheng, 2016), and modern energy storage technologies (Arunachalam et al., 2015). At the pore scale, flow is dominated by surface tension forces $\sigma$ and wall-wetting properties, and it is also strongly affected by the pore geometry. In fact, these types of systems are usually characterized by a small Eotvos number ($Eo = \Delta\rho g L^2/\sigma \ll 1$), that is, the largest drop, which may occupy the entire flow cross section, is still smaller than the critical (minimal) drop size required for merging of adjacent drops to take place, and, therefore, the flow characteristics are similar to microgravity systems (see Brauner, 1990).

The most common approach to modeling immiscible two-phase flow in a porous medium is to consider an extension of Darcy's law (Darcy, 1856) for the multiphase flow scenario by introducing the concept of relative permeabilities at the continuum scale. The main assumption of a linear relation between the filtration velocity and the pressure gradient is still considered valid, while the capillary pressure relation and a conservation law for the saturation are necessary to close the problem. The two-phase Darcy's law has been obtained both empirically (in analogy with single-phase flow; Bear, 1972; Leverett, 1941; Wyckoff & Botset, 1936) and has been derived theoretically by upscaling the Stoke's equation at the pore scale. Many upscaling approaches have been adopted so far, such as homogenization via multiple-scale expansions, (Auriault, 1987; Auriault et al., 1989; Daly & Roose, 2015; Hornung, 1997) and volume-averaging methods (Hassanizadeh & Gray1980, 1990, 1993a, 1993b; Kalaydjian, 1987; Marle, 1982; Slattery, 1968, 1970; Whitaker, 1986, just to mention a few). The issue of including inertia effects has been mostly studied for single-phase flow (see, for example, Z. Chen et al., 2001; Marusic-Paloka & Mikelic, 2000; Mei & Auriault, 1991; Sanchez-Palencia, 1980), although, in the context of multiphase flow, Lasseux et al. (2008) proposed an extension of the volume-averaged upscaled equations to account for inertial effects.

More recently, the classical interpretation of the macroscopic laws has been questioned (Niessner et al., 2011; Nordbotten et al., 2007, 2008; Xu & Wang, 2014), while their limited predictive capability has been long known and associated with the inherent assumptions of the multiphase Darcy law (Blunt, 2017). Quoting

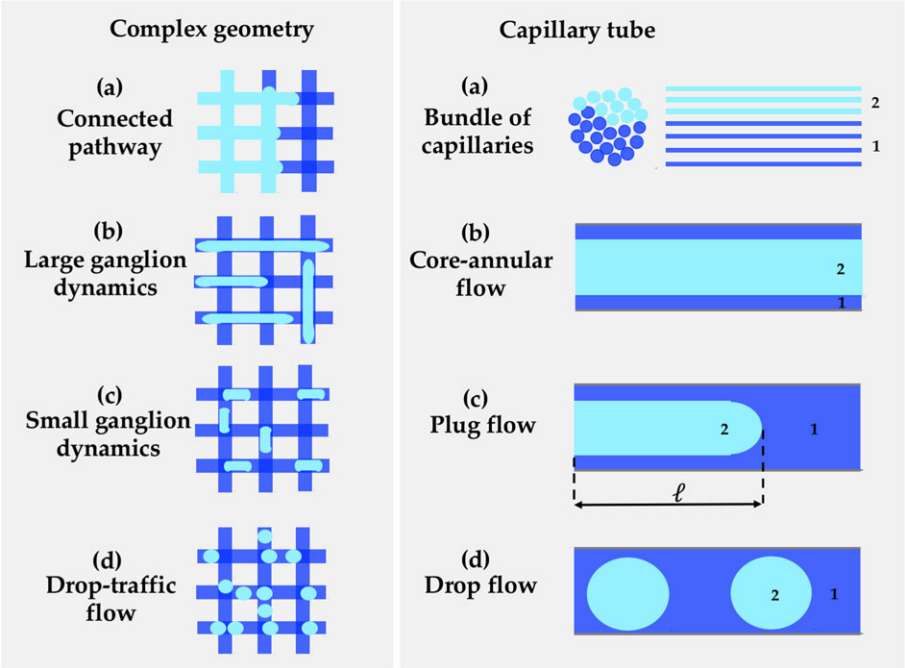


**Figure 1.** Sketch of flow regimes in a complex geometry and their idealization in a capillary tube of diameter *D* and length *L*. The wetting phase (dark blue) is referred to as phase 1, with the nonwetting phase (light blue) as phase 2.

from (Blunt, 2017,§6.3.2, pp. 255) "the key assumption inherent in the multiphase Darcy law is that we have a percolation-like displacement pattern, such that there is a representative elementary volume within which we have an average saturation that evolves slowly in both space and time. Over the time-scale for flow across this elementary volume, the saturation is approximately constant (that is there is little displacement), the fluid configuration is fixed and the relative permeabilities are the flow conductances of each phase …". With the advent of high-performance computing, it became increasingly possible to investigate pore-scale dynamics of immiscible displacement and understand its underlying physics (see, for example, Armstrong et al., 2016; McClure et al., 2016a; Tartakovsky & Meakin, 2006). This, despite the fact that the inherent instability of multiphase flows, and lack of reproducibility of controlled experiments (Ling et al., 2017), renders multiphase systems particularly challenging to model virtually at any scale. Concurrent improvements of X-ray microtomography combined with its nondestructive features have allowed direct visualization of pore-scale structures and distribution of phases as inputs to computational models. A number of authors have investigated pore-scale phases distribution using X-ray microtomography and demonstrated the complexity of the nonwetting and wetting phase interface geometry (e.g., Armstrong et al., 2014; Blunt et al., 2013; X. Chen & DiCarlo, 2016; X. Chen et al., 2017; Gao et al., 2017; Garing et al., 2017; Moghadasi et al., 2016; Prodanovic et al., 2007, 2015; Reynolds et al., 2017).

In fact, four possible steady state pore-scale flow regimes, that is, the microscale phase topology, have been experimentally identified by Avraam and Payatakes (1995a) for two-phase in porous media: large-ganglion dynamics, small-ganglion dynamics, drop traffic flow, and connected-pathway flow (see Figure 1, left). In large and small ganglion dynamics the wetting phase is continuous, while the nonwetting phase is disconnected and flows in the form of ganglia, much bigger (large ganglion) or smaller (small ganglion) than the average pore size. In the drop traffic flow regime, the nonwetting phase is disconnected and flows in the form of drops whose size is comparable to the average pore size, while in the connected-pathway regime both phases flow through separate and uninterrupted pathways. This flow regimes classification refers to quasi-static flow conditions at the pore scale and is motivated by the emerging evidence that the transition from connected pathways regime to an intermittent regime (e.g., ganglion-dynamics) can be identified as one of the causes of hysteric behavior of the relative permeability curves, (see Armstrong et al., 2016, 2017; Datta et al., 2014; Rucker et al., 2015).

In this work, we focus primarily on capturing the physical mechanisms (e.g., interfacial stresses) underlying the different flow regimes and their impact on relative permeability curves at steady state flow conditions. Unlike other studies, we do not focus on any dynamical effects and their impact on the capillary pressure relations nor on the transient evolution of the relative permeability during drainage or imbibition at unsteady flow conditions (Amir et al., 2015; Karadimitriou et al., 2014; Kianinejad et al., 2016); instead, we propose an approach to quantify the role that interfacial area has on relative permeabilities and the form of the upscaled equations. The importance of accounting for the evolution of the fluid-fluid interface has been already recognized, and different upscaling methods have been used to explicitly derive macroscopic equations for the evolution of the interface, (e.g., Gray et al., 2015; Gray & Miller, 2010; Hilfer, 1998; Jackson et al., 2009; McClure et al., 2016b; Niessner & Hassanizadeh, 2008; Rybak et al., 2015), while Karadimitriou et al. (2014) show how to estimate the interfacial variables in the macroscopic equations from experimental measurements of transient flow. However, the additional complexity in handling such models has hindered their penetration into real world applications, and routine calculations are still based on classical two-phase Darcy's law.

In this paper, we tackle this problem by proposing a homogenization approach based on the postulation of steady state pore-scale flow regimes, for example, ganglion dynamics and connected-pathway flow. We specifically aim at incorporating the interaction between the flowing phases and the solid by deriving upscaled equations that are regime-specific. The main advantage of the proposed approach lies in accounting for the effect of the phase-topology at the pore scale while retaining simplicity of the final formulation. Specifically, we use an analogy between such flow regimes in a real porous medium and two-phase flow in a capillary tube (see Figure 1, right, where the complexity due to the geometry is reduced but the physics behind the interaction between the phases is retained). We demonstrate that by postulating the flow regime (i.e., how the phases are displaced in space and time at the pore-scale), we are able to construct the effective parameters of the upscaled equations and to derive analytical expressions for the relative permeability of the wetting and the nonwetting phases for each flow regime. Following this approach, the interfacial area enters the upscaled model via the postulation of the pore-scale flow regime and it is naturally embedded in the macroscale equations through the relative permeabilities. Generalizations to realistic porous media is currently under investigation.

The paper is organized as follows. In section 2 we formulate the pore-scale problem of two-phase flow in a porous medium and we identify the relevant dimensionless parameters, that is, Eotvos, Reynolds, capillary, Froude numbers, and the viscosity and density ratio of the system. In section 3, first we present limitations and applicability conditions for the classical two-phase Darcy's law (section 3.1), and then we derive a new set of macroscopic equations by upscaling the incompressible Navier-Stokes equation by means of multiscale expansions, while specifying sufficient conditions that guarantee its validity. Differently from previous works, the macroscopic equation (section 3.2) has the form of the mechanical energy balance equation and it includes both unsteady and inertial effects, while the proposed closures are formulated for different flow regimes at the pore-scale (section 4). We discuss in detail the impact of the most common pore-scale flow regimes on the upscaled equations, namely, connected pathway and ganglion dynamics, and obtain analytical expressions for the relative permeabilities of the wetting and nonwetting phases for flow in a capillary tube. In addition, we show that two-phase Darcy's law represents only a particular case of the upscaling method presented here. The conclusions are summarized in section 5.

## 2. Problem Formulation

We consider the flow of two immiscible and incompressible fluids through a rigid porous medium $\hat{\Omega}$, formed by the spatial repetition of periodic unit cells $\hat{Y}$. Let $L$ and $l$ be the characteristic length scales of the medium and of the unit cell, respectively. The scale parameter is defined as $\varepsilon := l/L \ll 1$. The unit cell consists in the pore space occupied by the two fluids, $\hat{\mathcal{B}} = \hat{\mathcal{B}}_1 \cup \hat{\mathcal{B}}_2$, and the solid matrix $\hat{\mathcal{G}}$; the fluid-fluid interface is $\hat{\Gamma}_{12}$, while the fluid-wall interfaces are $\hat{\Gamma}_1$ and $\hat{\Gamma}_2$, respectively. The unit cells are connected, that is, the pore space $\hat{\mathcal{B}}$ of each cell $\hat{Y}$ forms the multiconnected pore-space domain $\hat{\mathcal{B}}^\varepsilon \subset \hat{\Omega}$, and the cell geometry (the spatial distribution of $\hat{\mathcal{G}}$) is considered known.

### 2.1. Governing Equations and Boundary Conditions

The flow of each (Newtonian) phase is described by the continuity and the Navier-Stokes equations in its fluid domain,

$$\hat{\nabla} \cdot \hat{\boldsymbol{u}}_i = 0, \quad \hat{\boldsymbol{x}} \in \hat{\mathcal{B}}_i, \tag{1a}$$

$$\rho_i \left[ \frac{\partial \hat{\boldsymbol{u}}_i}{\partial \hat{t}} + \left( \hat{\boldsymbol{u}}_i \cdot \hat{\nabla} \right) \hat{\boldsymbol{u}}_i \right] = -\hat{\nabla} \hat{p}_i + \mu_i \hat{\nabla}^2 \hat{\boldsymbol{u}}_i + \rho_i g \boldsymbol{e}_g, \quad \hat{\boldsymbol{x}} \in \hat{\mathcal{B}}_i, \tag{1b}$$

where $\hat{\boldsymbol{u}}_i(\hat{\boldsymbol{x}}, \hat{t})$, $\hat{p}_i(\hat{\boldsymbol{x}}, \hat{t})$, $\rho_i$, and $\mu_i$ are the velocity, the pressure, the density, and the dynamic viscosity of the $i$th phase; the subscript $i = 1, 2$ refers to the fluid 1 (wetting phase) and 2 (nonwetting phase), respectively, while $g$ is the gravitational acceleration and $\boldsymbol{e}_g$ is a unit vector whose direction aligns with gravity. The flow is subjected to no-slip and no-penetration at the walls,

$$\hat{\boldsymbol{u}}_i = 0 \quad \text{and} \quad \hat{\boldsymbol{u}}_i \cdot \boldsymbol{n} = 0 \quad \text{on} \quad \hat{\Gamma}_i, \tag{2}$$

and the continuity of velocity, normal, and tangential shear stresses at the fluid-fluid interface,

$$\hat{\boldsymbol{u}}_1 = \hat{\boldsymbol{u}}_2 \quad \text{on} \quad \hat{\Gamma}_{12}, \tag{3a}$$

$$\left( \hat{p}_1 - \hat{p}_2 \right) \boldsymbol{I} + \boldsymbol{n} \cdot \left[ \mu_1 \left( \hat{\nabla} \hat{\boldsymbol{u}}_1 + \hat{\nabla} \hat{\boldsymbol{u}}_1^T \right) - \mu_2 \left( \hat{\nabla} \hat{\boldsymbol{u}}_2 + \hat{\nabla} \hat{\boldsymbol{u}}_2^T \right) \right] \cdot \boldsymbol{n} = -\sigma \hat{\kappa} \quad \text{on} \quad \hat{\Gamma}_{12}, \tag{3b}$$

$$\boldsymbol{t} \cdot \left[ \mu_1 \left( \hat{\nabla} \hat{\boldsymbol{u}}_1 + \hat{\nabla} \hat{\boldsymbol{u}}_1^T \right) - \mu_2 \left( \hat{\nabla} \hat{\boldsymbol{u}}_2 + \hat{\nabla} \hat{\boldsymbol{u}}_2^T \right) \right] \cdot \boldsymbol{n} = 0 \quad \text{on} \quad \hat{\Gamma}_{12}, \tag{3c}$$

where $\sigma$ is the surface tension, $\hat{\kappa}(\hat{\boldsymbol{x}}, \hat{t}) = (1/R_1 + 1/R_2)$ is the local curvature of the interface, and $\boldsymbol{I}$ is the identity matrix, while $\boldsymbol{n}$ and $\boldsymbol{t}$ are the normal and tangential versors at the fluid-fluid interface $\hat{\Gamma}_{12}(\hat{\boldsymbol{x}}, \hat{t})$ which, advected by the flow, satisfies a kinematic boundary condition. In this analysis, its location (history of the interface) is supposed to be known.

### 2.2. Dimensionless Formulation

We normalize the governing equations by introducing the dimensionless quantities

$$\boldsymbol{x} = \frac{\hat{\boldsymbol{x}}}{L}, \quad t = \frac{\hat{t}}{L/U}, \quad p = \frac{\hat{p}}{\mu_1 UL/l^2}, \tag{4}$$

where $U$ is a characteristic velocity scale. It is worth emphasizing that the scaling of pressure is based on the assumption that pressure is the driving force at the macroscale and the viscous term and the pressure gradient in equation (1b) are of the same order of magnitude. This choice ensures that the energy introduced in the system at the larger scale (with characteristic length $L$) is dissipated at the pore scale (with characteristic length $l$), similarly to Auriault and Adler (1995) and Battiato and Tartakovsky (2011). This choice is important for determining the structure of the macroscopic equations, and, in particular, the capillary pressure relation. Rewriting the equations in terms of dimensionless variables, we obtain

$$\nabla \cdot \boldsymbol{u}_i = 0, \quad \boldsymbol{x} \in \mathcal{B}_i, \tag{5a}$$

$$\varepsilon^2 Re \left[ \frac{\partial \boldsymbol{u}_1}{\partial t} + \left( \boldsymbol{u}_1 \cdot \nabla \right) \boldsymbol{u}_1 \right] = -\nabla p_1 + \varepsilon^2 \nabla^2 \boldsymbol{u}_1 + \varepsilon^2 \frac{Re}{Fr^2} \boldsymbol{e}_g, \quad \boldsymbol{x} \in \mathcal{B}_1, \tag{5b}$$

$$\varepsilon^2 RRe \left[ \frac{\partial \boldsymbol{u}_2}{\partial t} + \left( \boldsymbol{u}_2 \cdot \nabla \right) \boldsymbol{u}_2 \right] = -\nabla p_2 + \varepsilon^2 M \nabla^2 \boldsymbol{u}_2 + \varepsilon^2 R \frac{Re}{Fr^2} \boldsymbol{e}_g, \quad \boldsymbol{x} \in \mathcal{B}_2, \tag{5c}$$

where

$$Re = \frac{\rho_1 UL}{\mu_1}, \quad Fr = \frac{U}{\sqrt{gL}}, \quad M = \frac{\mu_2}{\mu_1}, \quad \text{and} \quad R = \frac{\rho_2}{\rho_1} \tag{6}$$

are the Reynolds and the Froude numbers and the viscosity and density ratio, respectively. The dimensionless boundary conditions are

$$\boldsymbol{u}_i = 0 \quad \text{on} \quad \Gamma_i, \tag{7a}$$

$$\boldsymbol{u}_i \cdot \boldsymbol{n} = 0 \quad \text{on} \quad \Gamma_i, \tag{7b}$$

$$\boldsymbol{u}_1 - \boldsymbol{u}_2 = 0 \quad \text{on} \quad \Gamma_{12}, \tag{7c}$$

$$\left( p_1 - p_2 \right) \boldsymbol{I} + \varepsilon^2 \boldsymbol{n} \cdot \left[ \left( \nabla \boldsymbol{u}_1 + \nabla \boldsymbol{u}_1^T \right) - M \left( \nabla \boldsymbol{u}_2 + \nabla \boldsymbol{u}_2^T \right) \right] \cdot \boldsymbol{n} = -\frac{\varepsilon}{Ca} \kappa \quad \text{on} \quad \Gamma_{12}, \tag{7d}$$

$$\boldsymbol{t} \cdot \left[ \left( \nabla \boldsymbol{u}_1 + \nabla \boldsymbol{u}_1^T \right) - M \left( \nabla \boldsymbol{u}_2 + \nabla \boldsymbol{u}_2^T \right) \right] \cdot \boldsymbol{n} = 0 \quad \text{on} \quad \Gamma_{12}, \tag{7e}$$

where

$$Ca = \frac{\mu_1 U}{\sigma} \quad \text{and} \quad \kappa = \left( \frac{l}{R_1} + \frac{l}{R_2} \right) \tag{8}$$

are the capillary number and the dimensionless local curvature of the interface, respectively. We emphasize that since the local curvature is normalized by the characteristic length at the microscale (i.e., pore-scale), $\kappa$ is of order 1 only when the curvature radius is of the same order of the pore-scale characteristic length.

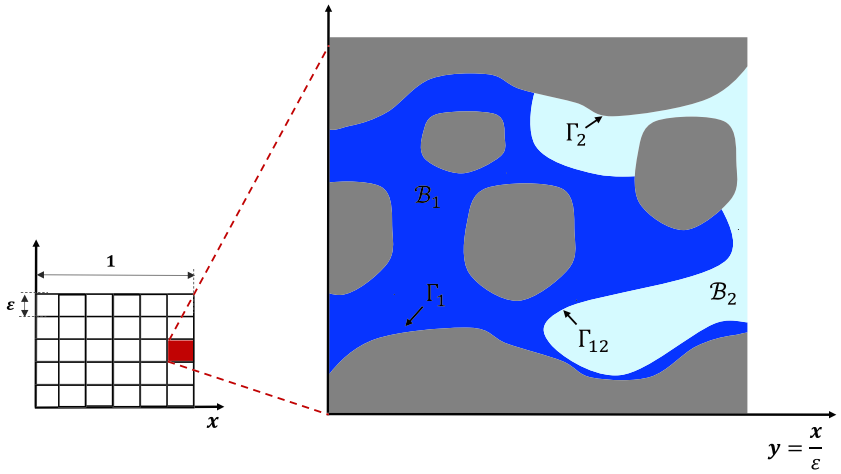


**Figure 2.** Schematic of the macroscopic domain and the unit cells defined in the homogenization process. A unit cell can be arbitrarily complex.

## 3. Homogenization via Multiple-Scale Expansions

The aim of the homogenization via multiple-scale expansions is to derive upscaled equations for averaged variables at the continuum scale (Darcy scale), which are representative of the flow at the pore scale. The main assumption is that separation of scales holds: two spatial scales, $L$ and $l$, exist such that $l \ll L$. It is assumed also that no other significant spatial scale influences the problem (see Figure 2): even though this hypothesis may be too restrictive when considering multiphase flow in a porous medium (i.e., the presence of a very thin film of one of the two fluids on the solid surface or complex structures bigger than the unit cell may easily violate the previous hypothesis), this type of analysis allows one to incorporate the shear interaction between phases at the pore scale.

Following Xu and Wang (2014), we assume that all the time-dependent variables depend only on the fast time scale $s = t/\varepsilon$, that is, the variation in time is significant only at the pore scale and $\partial/\partial t = 1/\varepsilon\ \partial/\partial s$. Then, we define the local averages of any arbitrary pore-scale quantity $\mathcal{X}(\boldsymbol{x}, s)$ in space (e.g., over the entire unit cell $Y$, the volume $\mathcal{B}_i$, or the surface $\Gamma$) and in time (over the time period $T$) as follows

$$\langle \mathcal{X} \rangle = \frac{1}{|Y|}\int_{\mathcal{B}_i} \mathcal{X} \mathrm{d}\boldsymbol{y}, \quad \langle \mathcal{X} \rangle_{\mathcal{B}_i} = \frac{1}{|\mathcal{B}|}\int_{\mathcal{B}_i} \mathcal{X} \mathrm{d}\boldsymbol{y}, \quad \langle \mathcal{X} \rangle_{\Gamma} = \frac{1}{|\Gamma|}\int_{\Gamma} \mathcal{X} \cdot \boldsymbol{n} \mathrm{d}\boldsymbol{y}, \quad \bar{\mathcal{X}} = \frac{1}{T}\int_{T} \mathcal{X} \mathrm{d}s, \tag{9}$$

where $\langle \mathcal{X} \rangle = S_i \phi \langle \mathcal{X} \rangle_{\mathcal{B}_i}$ and $|\mathcal{B}| = \phi |Y|$, with $\phi$ the porosity of the medium and $S_i$ the saturation of the $i$th phase, defined as

$$S_i = \frac{1}{\mathcal{B}}\int_{\mathcal{B}_i} \mathrm{d}\boldsymbol{y}. \tag{10}$$

The variables of the system are expanded in an asymptotic series in integer powers of $\varepsilon$ as

$$\begin{aligned} \boldsymbol{u}_i(\boldsymbol{x}, s) &= \boldsymbol{u}_i^{(0)}(\boldsymbol{x}, \boldsymbol{y}, s) + \varepsilon \boldsymbol{u}_i^{(1)}(\boldsymbol{x}, \boldsymbol{y}, s) + \dots \\ p_i(\boldsymbol{x}, s) &= p_i^{(0)}(\boldsymbol{x}, \boldsymbol{y}, s) + \varepsilon p_i^{(1)}(\boldsymbol{x}, \boldsymbol{y}, s) + \dots \\ \kappa_1(\boldsymbol{x}, s) &= \kappa_1^{(0)}(\boldsymbol{x}, \boldsymbol{y}, s) + \varepsilon \kappa_1^{(1)}(\boldsymbol{x}, \boldsymbol{y}, s) + \dots \end{aligned} \tag{11}$$

where

$$\boldsymbol{y} = \boldsymbol{x}/\varepsilon \tag{12}$$

is a fast variable and $j = \{0, 1, 2 \cdots\}$ and $i = \{1, 2\}$. The variables $\boldsymbol{u}_i^{(j)}(\boldsymbol{x}, \boldsymbol{y}, s)$, $p_i^{(j)}(\boldsymbol{x}, \boldsymbol{y}, s)$, and $\kappa_1^{(j)}(\boldsymbol{x}, \boldsymbol{y}, s)$, are $Y$-periodic functions in $\boldsymbol{y}$. This requirement is satisfied in case of steady state flow, but it is not always valid for displacement fronts that lack such periodicity. In these circumstances, the system may not be homogenizable across the displacement front and hybrid methods, where continuum-scale descriptions away from the front coupled to pore-scale equations across the front may be warranted. Although hybrid multiscale (or multialgorithm) methods in the context of porous media were initially introduced to model sharp reacting fronts in single-phase flow (Alexander et al., 2005; Battiato et al., 2011; Yousefzadeh & Battiato, 2017), where

continuum-scale approximations are rendered invalid (Auriault & Adler, 1995; Boso & Battiato, 2013; Korneev & Battiato, 2016), recent computational efforts, based on multialgorithm coupling, have focused on modeling displacement fronts in multiphase flows as well (e.g., Tomin & Lunati, 2013).

Furthermore, we define the upscaled set of equations in terms of the order of magnitude of the dimensionless numbers

$$Re = \varepsilon^{\alpha}, \quad Fr = \varepsilon^{\beta}, \quad R = \varepsilon^{\gamma}, \quad M = \varepsilon^{\delta}, \quad Ca = \varepsilon^{\eta}, \quad \kappa = \kappa_1(\boldsymbol{x}, s)\varepsilon^{\theta}, \tag{13}$$

where the exponents characterize the system behavior. In (13), $\kappa_1(\boldsymbol{x}, s)$ is the local curvature of the interface, defined as a term of order 1, $O(\kappa_1(\boldsymbol{x}, s)) = O(1)$, while the exponent $\theta$ indicates the magnitude of the curvature. This emphasizes the importance of treating the average curvature as one of the dimensionless parameters which need to be considered for classifying the system. From the practical point of view, we expect $\kappa$ to scale with the pore size for well connected phases, while it may scale differently for other pore-scale flow regimes.

In the following, we first derive the applicability conditions of the classical two-phase Darcy (section 3.1) and then present the regime-specific upscaled equations (section 3.2). Details of the derivations are presented in Appendices A, B, and C.

### 3.1. Limitations of the Two-Phase Darcy's Law

Despite the fact that the two-phase Darcy's law is extensively used for routine macroscopic calculations, to the best of our knowledge, a rigorous definition of its applicability regimes has not yet been provided in the literature, except for the experimental classification presented by (Cinar & Riaz, 2014). Here, differently from previous analyses (e.g., Auriault, 1987; Auriault et al., 1989; Hornung, 1997), we reformulated the derivation in terms of dimensionless variables, see Appendix B for all the details, obtaining the filtration laws

$$\langle \boldsymbol{u}_1 \rangle = -\mathbf{K}_{11}\nabla p_1 - \mathbf{K}_{12}\nabla p_2, \qquad \boldsymbol{x} \in \Omega, \tag{14a}$$

$$\langle \boldsymbol{u}_2 \rangle = -\mathbf{K}_{21}\nabla p_1 - \mathbf{K}_{22}\nabla p_2, \qquad \boldsymbol{x} \in \Omega, \tag{14b}$$

along with the relation between the macroscopic pressures of the two phases

$$p_1 - p_2 = \langle \kappa \rangle \tag{15}$$

and the conservation laws for the saturation

$$\phi \frac{\partial S_i}{\partial t} + \nabla \cdot \langle \boldsymbol{u}_i \rangle = 0 \quad \text{with} \quad i = 1, 2 \quad \text{and} \quad S_1 + S_2 = 1. \tag{16}$$

Equations (14)-(16) are recovered only if the following conditions are met:

1. $\varepsilon \ll 1$;
2. $Re < \varepsilon^{-1}$ and $R \cdot Re < \varepsilon^{-1}$;
3. $Re/Fr^2 > \varepsilon^{-2}$ and $R \cdot Re/Fr^2 > \varepsilon^{-2}$;
4. $O(M) = 1$;
5. $O(\langle \kappa \rangle / Ca) = \varepsilon^{-1}$;
6. the interface $\Gamma_{12}$ is almost stationary.

In equation (14), $\mathbf{K}_{ij}$ are the dimensionless permeability tensors formally defined during the homogenization process as the average of closure variables, $\mathbf{K}_{ij} = \langle \boldsymbol{k}_{ij}(\boldsymbol{y}) \rangle$ (see Appendix B1), while in equation (15), $\langle \kappa \rangle$ represents the average pore-scale curvature of the system.

The constraints 1–5 ensure the separation of scales and define the applicability of the Darcy's law for two-phase law depending on the relative importance of Reynolds number, the density ratio, the viscosity ratio, the capillary number, and the average pore-scale curvature of the system. We have summarized the conditions for which the macroscopic equations hold in the phase diagrams of Figure 3. The colored region of Figure 3a (constraint 2) indicates conditions for which the unsteady and inertia effects are negligible for both phases in terms of $Re$ and $R$. Figure 3b (constraint 3) summarizes conditions for a microgravity system (i.e., the gravity contribution is negligible for both phases) in terms of $Re/Fr^2$ and $R$: since two-phase flows in porous media are characterized by a small Eotvos number ($Eo \ll 1$), this constraint is often met in practical cases. As imposed by constraint 4, the viscosity ratio should be of order 1 to ensure both the separation of scales and the existence of a filtration law for phase 2.

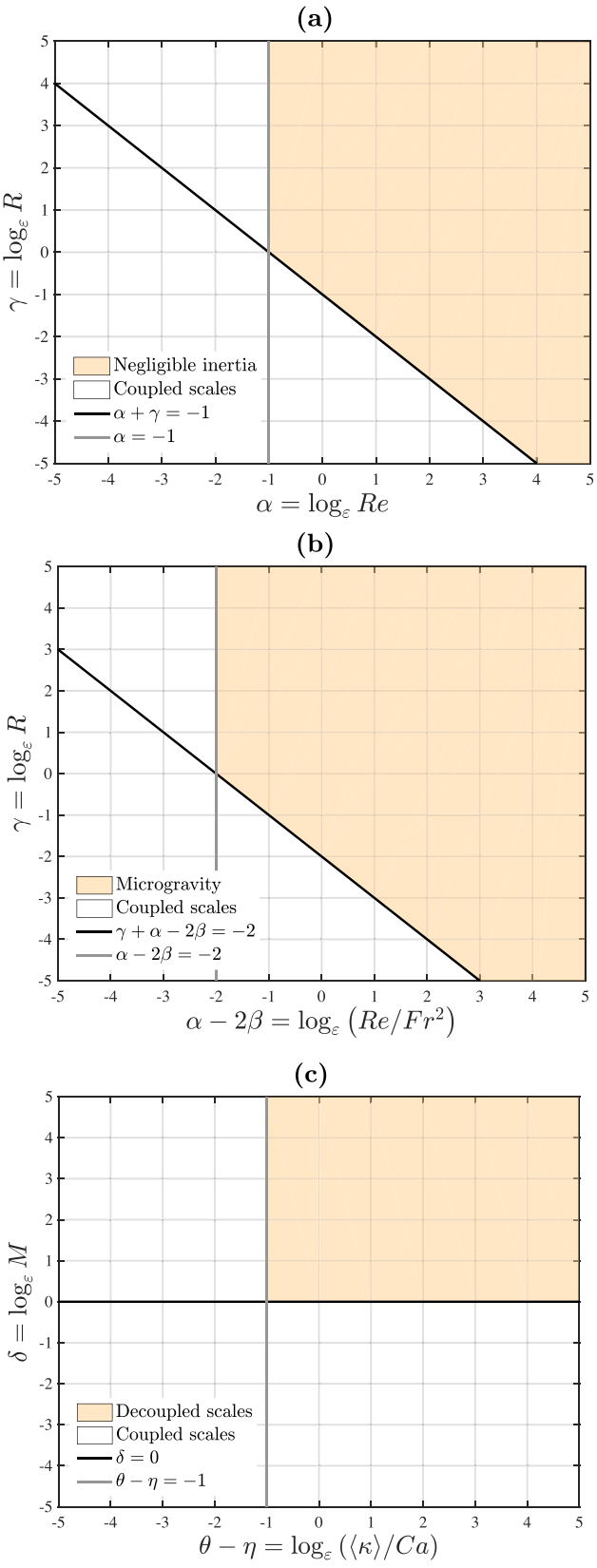


**Figure 3.** Phase diagram indicating the applicability of the macroscopic equations for two-phase flow in a porous media in terms of (a) *Re* and *R*; (b) $Re/Fr^2$ and *R*; (c) $\langle\kappa\rangle/Ca$ and *M*.

Interestingly, we show that the capillary number alone is not sufficient to guarantee that scales are separated: instead, the ratio of the average pore-scale curvature, $\langle\kappa\rangle$, to the capillary number *Ca* (see Figure 3c) needs to satisfy appropriate conditions. Specifically, equation (15) is recovered only if such ratio is of order of $\varepsilon^{-1}$. From a practical point of view, the average pore-scale curvature radius for well-connected phases scales with the pore size, namely, $O(\langle\kappa\rangle) = O(1)$, and, therefore, the inequality of the macroscopic pressures is recovered only when $O(Ca) = O(\varepsilon)$. This may not be true for different flow regimes (e.g., ganglion and drop traffic flows), where pore-scale curvature may not always be well defined. Thus, a correct estimation of the average pore-scale curvature, and consequently of pore-scale flow regimes, is an essential information for classifying the system, as pointed out also by the recent experimental analysis by Armstrong et al. (2012) and Singh et al. (2016).

The calculation of relative permeabilities by solving the closure problem is complex and computationally expensive in the context of two-phase flow, and, therefore, deriving consistent expressions for $\boldsymbol{K}_{ij}$ is not straightforward. Yet, experimental evidence suggests that relative permeabilities should be dramatically influenced by pore-scale flow regimes, since significant changes in phase connectivity and the generation of intermittent structures of the nonwetting phase (ganglia) may be one of the leading causes of hysteretic behavior of relative permeability curves (see Armstrong et al., 2016; Avraam & Payatakes, 1995a). Thus, incorporating the physical dependence of the pore scale processes in to upscaled equation is the main motivation behind the a new upscaling approach proposed here.

In the following, we address this problem by deriving an upscaled equation for the mechanical energy balance, where the closures are developed for specific flow regimes.

### 3.2. Upscaled Mechanical Energy Balance for Two-Phase Flow in Porous Media

In this section, we present a general set of upscaled equations which we have obtained by homogenization of the two-phase Navier-Stokes problem while embedding also unsteady and inertia effects (all the details of the derivation are shown in Appendix C). The upscaled equations are cast in the form of a mechanical energy balance: here the objective is to retain both the simplicity of the final formulation and the capability to easily incorporate multiphase pore-scale dynamics. We obtain that the momentum transfer between two phases in a rigid porous medium, described by equations (5), can be homogenized as follows:

$$\varepsilon Re\left(\mathcal{A}_1 + \mathcal{F}_1\right) = -\nabla p_1 \cdot \langle\overline{\boldsymbol{u}}_1\rangle - \mathcal{P}_1 + \mathcal{W}_1 + \varepsilon^2 \frac{Re}{Fr^2}\mathcal{G}_1, \qquad \boldsymbol{x} \in \Omega, \quad (17a)$$

$$\varepsilon ReR\left(\mathcal{A}_2 + \mathcal{F}_2\right) = -\nabla p_2 \cdot \langle\overline{\boldsymbol{u}}_2\rangle - \mathcal{P}_2 + M\mathcal{W}_2 + \varepsilon^2 R\frac{Re}{Fr^2}\mathcal{G}_2, \qquad \boldsymbol{x} \in \Omega, \quad (17b)$$

$$p_1 - p_2 = \frac{\langle\overline{\kappa}\rangle}{Ca}\varepsilon, \quad (17c)$$

where $\langle\overline{\kappa}\rangle$ represents the averaged pore-scale curvature, $p_1$ and $p_2$ are the macroscopic pressure, while $\langle\overline{\boldsymbol{u}}_1\rangle$ and $\langle\overline{\boldsymbol{u}}_2\rangle$ are the filtration velocity of the phase 1 and 2, respectively. In (17), (i) $\mathcal{A}_{1,2}$ is the unsteady term, it is associated with the accumulation of kinetic energy and vanishes for steady state flow; (ii) $\mathcal{F}_{1,2}$ is the Forchheimer term, which embeds inertia effects, and vanishes for fully developed flow; (iii) $\mathcal{W}_{1,2}$ is the work term which accounts for the shear stress at the wall and at the fluid-fluid interface in

the unit cell; and (iv) $\mathcal{P}_{1,2}$ is the pressure term; (v) $\mathcal{G}_{1,2}$ is the gravity term which accounts for the work done by the body force on the system. The problem is then closed with a conservation law for the saturation, that is, equation (16).

The capillary pressure relation (17c) is strongly controlled by the average curvature at the pore scale, $\langle\overline{\kappa}\rangle$, which can be estimated for both the cases of well-connected and unconnected phases, i.e., connected pathway and ganglia flow regimes, respectively. From a practical point of view, a complex phase topology can be accounted for because $\langle\overline{\kappa}\rangle$ is obtained by averaging the local curvature over the unit cell. For example, in the case of ganglion flow dynamics, the average pore-scale curvature radius does not necessarily scale with the pore size because, while the diameter of elongated drops is of the order of the pore size ($Eo \ll 1$ systems; Brauner, 1990), the drops do not necessarily occupy the entire unit cell. Therefore, if we know the phase topology along with other scaling parameters in the upscaled equations, we can fully determine the capillary pressure relation. In this regard, McClure et al. (2018) consider a geometrical description of the capillary pressure, which relates the average mean curvature, the fluid saturation, the interfacial area between fluids, and the Euler characteristic. They show that a geometric state function is able to characterize the microscopic fluid configurations. Such types of relationships between flow regimes and pore-scale topology of the interface would allow one to estimate the right-hand side (RHS) of (17c). In classical derivations, instead, the hypothesis of well-connected phases is required, and, only recently, different strategies have been proposed for handling the issue of unconnected phases by assigning a macroscopic volume averaged pressure to the nonwetting phase (Nordbotten et al., 2008) or by introducing new state variables for the nonconnected phases (Hilfer, 2006). Finally, we want to emphasize that from a physical point of view, equation (17c) should simply be interpreted as a relation between the macroscopic pressures, where the averaged pore-scale curvature includes both capillary and dynamic effects (see Løvoll et al., 2011).

The upscaled equations (17a) and (17b), hold when the following applicability conditions are satisfied (summarized in Figure 3):

1. $\varepsilon \ll 1$;
2. $R \cdot Re \leq \varepsilon^{-1}$ and $Re \leq \varepsilon^{-1}$ ;
3. $R \cdot Re/Fr^2 \geq \varepsilon^{-2}$ and $Re/Fr^2 \geq \varepsilon^{-2}$;
4. $O(M) \leq (1)$;
5. $\langle\overline{\kappa}\rangle/Ca \geq \varepsilon^{-1}$.

Compared to the case of the two-phase Darcy's law (see section 3.1), some constraints have been relaxed. First, here we can account for the case of nonnegligible inertia and unsteady effects, namely, the boundaries of the colored region in Figure 3a which correspond to $Re = 1/\varepsilon$ and $Re \cdot R = 1/\varepsilon$. In fact, both the unsteady and the Forchheimer terms in equation (17) are controlled by the order of magnitude of $Re$ and $R$. The shaded region of Figure 3c shows that the upscaled equations hold for a specific combination of the viscosity ratio $M$, which also controls the term $\mathcal{W}_2$, and the ratio of the average pore-scale curvature and the capillary number. In particular, we are including in the applicability region also the cases which give us the equality of the macroscopic pressures, that is, $\langle\overline{\kappa}\rangle/Ca > \varepsilon^{-1}$. Finally, Figure 3b summarizes the conditions to be satisfied for assuming a microgravity system.

In the following, using a capillary tube analogy, we formulate regime-specific closure relationships.

## 4. Impact of Pore-Scale Flow Regimes on the Upscaled Equation

In this section, we present the impact of pore-scale flow regimes on the upscaled equations: we first postulate the pore-scale flow regime (i.e., connected pathway, small ganglion, and large ganglion dynamics) and, then, we derive regime-specific upscaled equations from the one obtained in section 3.2 by modeling specific closures for each flow regime. To achieve this goal, we propose an analogy between flow regimes in a real porous medium, as experimentally observed by Avraam and Payatakes (1995a) and Armstrong et al. (2016) and the basic flow regimes in a straight capillary tube of diameter $D$ and length $L$ at microgravity conditions ($Eo \ll 1$ ) with porosity $\phi = 1$, as shown in Figure 1. In fact, a capillary tube can be assumed as the simplest representation of a porous medium (Bear, 1972), and, in the two-phase context, it results to be a convenient solution for modeling the friction at the solid walls and at the fluid-fluid interfaces for different flow regimes. Since we treat the system as one-dimensional, we only require that the scale parameter is sufficiently small, $\varepsilon = D/L \ll 1$, where the tube diameter is the pore-scale characteristics length. At the same time, we look at low Eotvos num-

ber systems: in these conditions, the phase topology is strongly affected by surface tension effects, and drops occupy almost the entire cross section of the microchannel (see Brauner, 1990; Yagodnitsyna et al., 2016).

In this context, the analogy allows us to significantly reduce the complexity of the problem, while retaining the fundamental physical interactions between the fluids. In particular, we look at the following flow regimes:

1. Connected-pathway flow: Both phases flow in separate and uninterrupted pathways, and, in steady state conditions, the interface between phases can be considered static (see Armstrong et al., 2016; Avraam & Payatakes, 1995a). In this flow regime the fluid-fluid interactions are negligible compared to fluid-wall interactions because each phase flows in separate pathways. As a result, the connected pathway flow is modeled as a bundle of capillary tubes; see case (a) in Figure 1.
2. Large-ganglion dynamics: The wetting phase is continuous, while the nonwetting phase is disconnected and flows in the form of ganglia significantly bigger than the average pore size. The analog of this flow regime is a core-annular flow in a capillary tube; see case (b) in Figure 1, where the length of the ganglion is much larger than a unit cell: the nonwetting phase flows surrounded by a film of wetting phase.
3. Small-ganglion dynamics: It is intrinsically an intermittent flow regime where small disconnected ganglia of the nonwetting phase have a size comparable to the average pore size. This flow regime can be idealized as plug flow (elongated drop flow) in a capillary tube, namely, a sequence of taps of a continuous phase and elongated drops, which are surrounded by a film of the continuous phase; see case (c) in Figure 1.
4. Drop traffic flow regime: The nonwetting phase is disconnected and flows in the form of a sequence drops whose size is comparable to the capillary tube diameter; see case (d) in Figure 1.

In the following sections, we first present the upscaled equations for the case of one-dimensional flow (section 4.1) including the limit of single phase flow, and then, we provide analytical closures for the aforementioned flow regimes (connected pathway, core-annular, and plug flow) in a capillary tube analog setting. The case of drop traffic flow will not be addressed here due to the absence, to the best of our knowledge, of specific closures to model drag of a viscous drop flowing in a microchannel. Such closures exist in the context of bubbly flow at large Eotvos number (Cazarez et al., 2010; Picchi, Strazza, et al., 2015a), where drops (or bubbles) have an average size much smaller than the pipe diameter. Since the phase topology at large Eotvos numbers is significantly different from the case investigated here (where the size of the bubbles is comparable to that of the channel), large Eotvos number closures cannot be directly applied to flow in microchannels. However, we expect the qualitative trend of the relative permeability curves for the drop traffic flow to be similar to the case of small ganglia (very short plug), even if deviations are expected due to the different geometry between drops (almost spherical) and short plugs.

### 4.1. One-Dimensional Macroscale Flows Equations

For one-dimensional flow, equation (17) can be simplified as follows (see Appendix C for the details)

$$\varepsilon Re\left(\frac{\mathcal{A}_1}{\langle\overline{\boldsymbol{u}}_1\rangle}+\frac{\phi\omega_1\mathcal{K}_1}{2}\langle\overline{\boldsymbol{u}}_1\rangle_{\mathcal{B}_1}^2\right)=-\nabla p_1+\phi\left(\mathcal{T}_{f1}+\mathcal{T}_{w1}\right)+\varepsilon^2\frac{Re}{Fr^2}e_g,\quad \boldsymbol{x}\in\Omega, \tag{18a}$$

$$\varepsilon ReR\left(\frac{\mathcal{A}_2}{\langle\overline{\boldsymbol{u}}_2\rangle}+\frac{\phi\omega_2\mathcal{K}_2}{2}\langle\overline{\boldsymbol{u}}_2\rangle_{\mathcal{B}_2}^2\right)=-\nabla p_2+M\phi\left(\mathcal{T}_{f2}+\mathcal{T}_{w2}\right)+\varepsilon^2R\frac{Re}{Fr^2}e_g,\quad \boldsymbol{x}\in\Omega, \tag{18b}$$

where $\mathcal{T}_{f1}$, $\mathcal{T}_{f2}$, $\mathcal{T}_{w1}$, and $\mathcal{T}_{w2}$ are the interfacial shear stress and the wall shear stress terms for phases 1 and 2, respectively. An advantage of this formulation is that we are able to isolate the contribution of fluid-fluid (interfacial terms) and fluid-wall (wall terms) interactions. As a result, incorporating the effects of pore-scale flow regimes in the upscaled equations reduces to modeling the shear-stress terms. Also, the inertia terms in the left-hand side (LHS) of equation (18) have been rewritten as a function of the square of the average velocity as a Forchheimer-type term (see Forchheimer, 1901). The parameters $\mathcal{K}_i$ and the shape factor $\omega_i$ are functions of the flow regimes at the pore scale, and they are defined as

$$\mathcal{K}_i=\frac{|\Gamma|}{|\mathcal{B}_i|},\qquad \omega_i=\frac{\langle\overline{\boldsymbol{u}_i^3}\rangle_\Gamma}{\langle\overline{\boldsymbol{u}}_i\rangle_{\mathcal{B}_i}^3}, \tag{19}$$

where $\Gamma$ is the surface which bounds the volume $\mathcal{B}_i$ of the $i$th phase in the unit cell. In case the phase topology and the velocity profiles at the inflow and outflow of the unit cell are known, $\mathcal{K}_i$ and $\omega_i$ are fully determined.

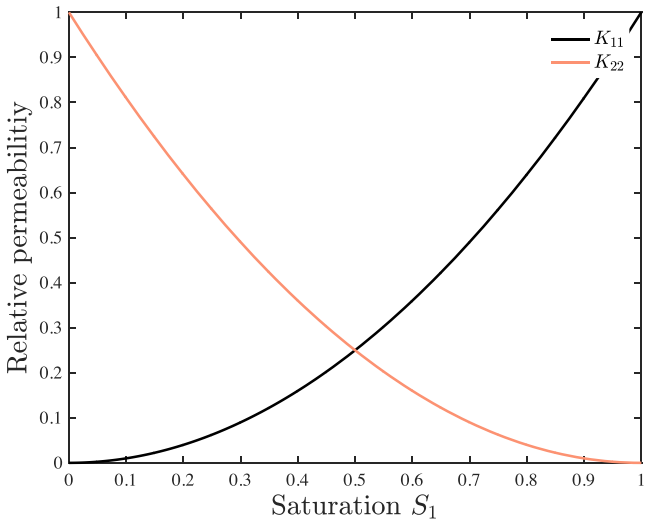


**Figure 4.** Relative permeabilities of the wetting phase, $K_{11}$, and the nonwetting phase, $K_{22}$, as a function of the saturation of the wetting phase, $S_1$, for the connected pathway flow.

#### 4.1.1. Single-Phase Limit

In this section we show that the classical formulation of the Darcy's law is easily recovered as a particular case of our approach. In fact, assuming one-dimensional and single-phase flow in a capillary tube of constant diameter $D$ and of length $L$ with $\varepsilon = D/L \ll 1$, equation (17) reduces to the classical Darcy's law

$$\varepsilon Re \mathcal{K} \omega \left\langle \overline{\boldsymbol{u}} \right\rangle_{\mathcal{B}}^2 = \varepsilon^2 \frac{Re}{Fr^2} e_g - \nabla p - 32 \langle \overline{\boldsymbol{u}} \rangle_{\mathcal{B}}. \tag{20}$$

In equation (20), the Forchheimer correction is proportional to the velocity shape factor $\omega$ and to $\mathcal{K} = 2(\varepsilon+2)$, which has been determined as the ratio of the surface and the volume of the (cylindrical) capillary tube. The wall stress term, defined in equation (C13) of Appendix C, is given by ($\mathcal{T}_f = 0$ for single-phase flow)

$$\mathcal{T}_w = \langle \overline{\boldsymbol{\tau}}_w \rangle_{\mathcal{B}} \frac{\Gamma_1}{\mathcal{B}} = -32 \langle \overline{\boldsymbol{u}} \rangle_{\mathcal{B}}. \tag{21}$$

The dimensionless ratio between the wetted surface and the volume occupied by the fluid is $\Gamma_1/\mathcal{B} = 4$, and the dimensionless averaged shear stress has been obtained from the single phase friction factor relation as

$$\langle \overline{\boldsymbol{\tau}}_w \rangle_{\mathcal{B}} = \frac{\langle \overline{\hat{\boldsymbol{\tau}}}_w \rangle_{\hat{\mathcal{B}}}}{\mu U/D}, \tag{22}$$

where

$$\langle \overline{\hat{\boldsymbol{\tau}}}_w \rangle_{\hat{\mathcal{B}}} = \frac{1}{2} f_w \langle \overline{\hat{\boldsymbol{u}}} \rangle_{\hat{\mathcal{B}}}^2, \quad f_w = \frac{16}{Re}, \quad Re = \frac{\rho \langle \overline{\hat{\boldsymbol{u}}} \rangle_{\hat{\mathcal{B}}} D}{\mu}. \tag{23}$$

### 4.2. Connected Pathway Flow

We would like to emphasize that since in this flow regime each capillary tube is occupied by one phase only (see Figure 1a), equation (18) cannot be employed (since it is derived under the hypothesis that both phases flow in the same capillary). Therefore, the connected pathway flow regime is upscaled considering a bundle of $N$ capillary tubes of constant diameter $D$ and length $L$ (see Figure 1), while assuming that the $i$th phase occupies $NS_i$ capillaries. This leads to

$$\langle \overline{\hat{\boldsymbol{u}}}_1 \rangle_{\hat{\mathcal{B}}_1} = -\frac{ND^2 S_1}{32\mu_1} \nabla \hat{p}_1, \tag{24a}$$

$$\langle \overline{\hat{\boldsymbol{u}}}_2 \rangle_{\hat{\mathcal{B}}_2} = -\frac{ND^2 (1-S_1)}{32\mu_2} \nabla \hat{p}_2, \tag{24b}$$

where $S_i$ is the saturation. Recalling that $\left\langle \overline{\boldsymbol{u}}_i \right\rangle = S_i \phi \left\langle \overline{\boldsymbol{u}}_i \right\rangle_{\mathcal{B}_i}$, the Darcy's law in dimensionless form becomes

$$\left\langle \overline{\boldsymbol{u}}_1 \right\rangle = -\frac{\phi K_{11}}{32} \nabla p_1 \quad \text{with} \quad K_{11} = S_1^2, \tag{25a}$$

$$\left\langle \overline{\boldsymbol{u}}_2 \right\rangle = -\frac{\phi K_{22}}{32M} \nabla p_2 \quad \text{with} \quad K_{22} = \left(1 - S_1\right)^2, \tag{25b}$$

where the length, the velocity, and the shear stress scales are the tube diameter $D$, $U$, and $\mu_1 UN/D$, respectively. The relative permeabilities $K_{11}$ and $K_{22}$ are plotted in Figure 4 as a function of the saturation of the wetting phase.

### 4.3. Core-Annular Flow in a Capillary Tube

Laminar core-annular flow is considered the basic flow regime in a capillary tube of diameter $D$ and length $L$ (with $\varepsilon = D/L \ll 1$; see Figure 1b): the wetting phase flows in the annulus while the nonwetting phase flows in the core. In this case, equations (18) yields

$$\varepsilon Re \mathcal{K}_1 \omega_1 \left\langle \overline{\boldsymbol{u}}_1 \right\rangle_{\mathcal{B}_1}^2 = -\nabla p_1 + 32 \left( M \frac{\langle \overline{\boldsymbol{u}}_2 \rangle_{\mathcal{B}_2} - 2 \langle \overline{\boldsymbol{u}}_1 \rangle_{\mathcal{B}_1}}{S_1} - \frac{\langle \overline{\boldsymbol{u}}_1 \rangle_{\mathcal{B}_1}}{S_1^2} \right), \tag{26a}$$

$$\varepsilon RRe\mathcal{K}_2\omega_2 \left\langle \overline{\boldsymbol{u}}_2 \right\rangle^2_{\mathcal{B}_2} = -\nabla p_2 + 32M\left(\frac{2\langle \overline{\boldsymbol{u}}_1\rangle_{\mathcal{B}_1} - \langle \overline{\boldsymbol{u}}_2\rangle_{\mathcal{B}_2}}{1-S_1}\right), \tag{26b}$$

where the subscripts 1 and 2 refer to the annulus (wetting phase) and core (nonwetting phase), respectively. In order to construct the final form of the upscaled equations for core-annular flows, we have adapted the closures commonly used in one-dimensional averaged models for pipe flow. Specifically, the shear stress terms in the upscaled equations (defined by equation (C13)) have been constructed similarly to the closures proposed by Ullmann and Brauner (2004): such closures, once implemented in a one-dimensional average model, reproduce the exact laminar solution at steady state and fully developed conditions (i.e., flat interface in the direction of the pipe axis). In the context of the proposed upscaling we obtain

$$\mathcal{T}_{f1} = -\langle \overline{\boldsymbol{\tau}}_f\rangle_{\mathcal{B}_1}\frac{\Gamma_{12}}{\mathcal{B}_1}, \quad \text{and} \quad \mathcal{T}_{w1} = \langle \overline{\boldsymbol{\tau}}_w\rangle_{\mathcal{B}_1}\frac{\Gamma_1}{\mathcal{B}_1}, \tag{27a}$$

$$\mathcal{T}_{f2} = \langle \overline{\boldsymbol{\tau}}_f\rangle_{\mathcal{B}_2}\frac{\Gamma_{12}}{\mathcal{B}_2}, \quad \text{and} \quad \mathcal{T}_{w2} = 0, \tag{27b}$$

where

$$\langle \overline{\boldsymbol{\tau}_w}\rangle_{\mathcal{B}_1} = \frac{\langle \overline{\hat{\boldsymbol{\tau}}}_w\rangle_{\hat{\mathcal{B}}_1}}{\mu_1 U/D}, \qquad \langle \overline{\boldsymbol{\tau}_f}\rangle_{\mathcal{B}_{1,2}} = \frac{\langle \overline{\hat{\boldsymbol{\tau}}}_f\rangle_{\hat{\mathcal{B}}_{1,2}}}{\mu_1 U/D} \tag{28}$$

are the average dimensionless shear stress at the wall and at the fluid-fluid interface, where

$$\langle \overline{\hat{\boldsymbol{\tau}}}_w\rangle_{\hat{\mathcal{B}}_1} = -\frac{1}{2}\rho_1 f_1 \langle \overline{\hat{\boldsymbol{u}}}_1\rangle^2_{\hat{\mathcal{B}}_1} \quad \text{with} \quad f_1 = \frac{16}{Re_1}, \quad Re_1 = \frac{\rho_1 \hat{D}_1 \langle \overline{\hat{\boldsymbol{u}}}_1\rangle_{\hat{\mathcal{B}}_1}}{\mu_1}, \tag{29a}$$

$$\langle \overline{\hat{\boldsymbol{\tau}}}_f\rangle_{\hat{\mathcal{B}}_{1,2}} = -\frac{1}{2}\rho_2 f_2 \langle \overline{\hat{\boldsymbol{u}}}_2\rangle_{\hat{\mathcal{B}}_2}\left(\langle \overline{\hat{\boldsymbol{u}}}_2\rangle_{\hat{\mathcal{B}}_2} - 2\langle \overline{\hat{\boldsymbol{u}}}_1\rangle_{\hat{\mathcal{B}}_1}\right) \quad \text{with} \quad f_2 = \frac{16}{Re_2}, \quad Re_2 = \frac{\rho_2 \hat{D}_2 \langle \overline{\hat{\boldsymbol{u}}}_2\rangle_{\hat{\mathcal{B}}_2}}{\mu_2}. \tag{29b}$$

$\hat{D}_1 = S_1 D$ and $\hat{D}_2 = \sqrt{1-S_1}D$ are the hydraulic diameters of phases 1 and 2, respectively. The dimensionless wetted surfaces and volume occupied by the $i$th phase are given by $\Gamma_1/\mathcal{B}_1 = 4/S_1$, $\Gamma_{12}/\mathcal{B}_1 = 4\sqrt{1-S_1}/S_1$, and $\Gamma_{12}/\mathcal{B}_2 = 4\sqrt{1-S_1}/(1-S_1)$.

In addition, since the core-annular flow regime has been postulated, Figure 1b, the coefficients in the Forchheimer terms (LHS of the upscaled equation (26)) can be modeled depending on the spatial distribution of the phases: the nonwetting phase occupies a cylinder of radius equal to the square of the saturation $\sqrt{S_2}$ and length $L$, while the wetting phase occupies the annulus of internal and external radii $\sqrt{S_2}$ and 1, respectively and of length $L$. The coefficients $\mathcal{K}_1$ and $\mathcal{K}_2$, which are the ratio between the surface and the volume occupied by each phase in the unit cell (see equation (19)), are fully determined, and are given by

$$\mathcal{K}_1 = 2\varepsilon + \frac{4(1+S_1)}{S_1}, \quad \text{and} \quad \mathcal{K}_2 = 2\varepsilon + 4, \tag{30}$$

while the shape factors $\omega_1$ and $\omega_2$ should be determined accordingly to equation (19) and depend on the velocity profiles at the inflow and the outflow sections of the unit cell; more technical details are available in Appendix C. For the particular case of fully developed core-annular flow, the shape factor integrals vanish since the contribution at the inflow boundary balances the one at the outflow boundary (the inlet and outlet velocity profiles are the same), but in the general case of not fully developed flow, they need to be modeled. Since their calculation requires information on the velocity profiles and the saturation, it is worth showing the trends of $\omega_1$ and $\omega_2$ in the limit of $L \to 0$, namely, the case of a cross-section of the capillary tube, where $\Gamma = \mathcal{B}_{1,2}$ (see Figure 5a). In this case, the shape factors can be analytically determined from their definition in equation (19) under the hypothesis of laminar velocity profiles of core-annular flow (the analytical solution for laminar can be found in Ullmann & Brauner, 2004). We obtain that $\omega_1$ (wetting phase) is constant and independent from the fluid saturation, that is, $\omega_1 = 2$, while $\omega_2$ (nonwetting phase) depends on the saturation and the viscosity ratio of the system. Furthermore, $\omega_2$ reaches the limiting values of 1 and 2 for the limit cases of vanishing nonwetting phase ($S_2 \to 0$) and thin film of wetting phase ($S_2 \to 1$) phase, respectively.

In absence of waviness at the interface (i.e., fully developed core-annular flow), the two phases have the same pressure gradient ($\nabla p_1 = \nabla p_2$), although they have different pressures due to the curvature of the interface in the cross section of the tube. As a result, since terms on the RHS of equations (26) are linear with respect to

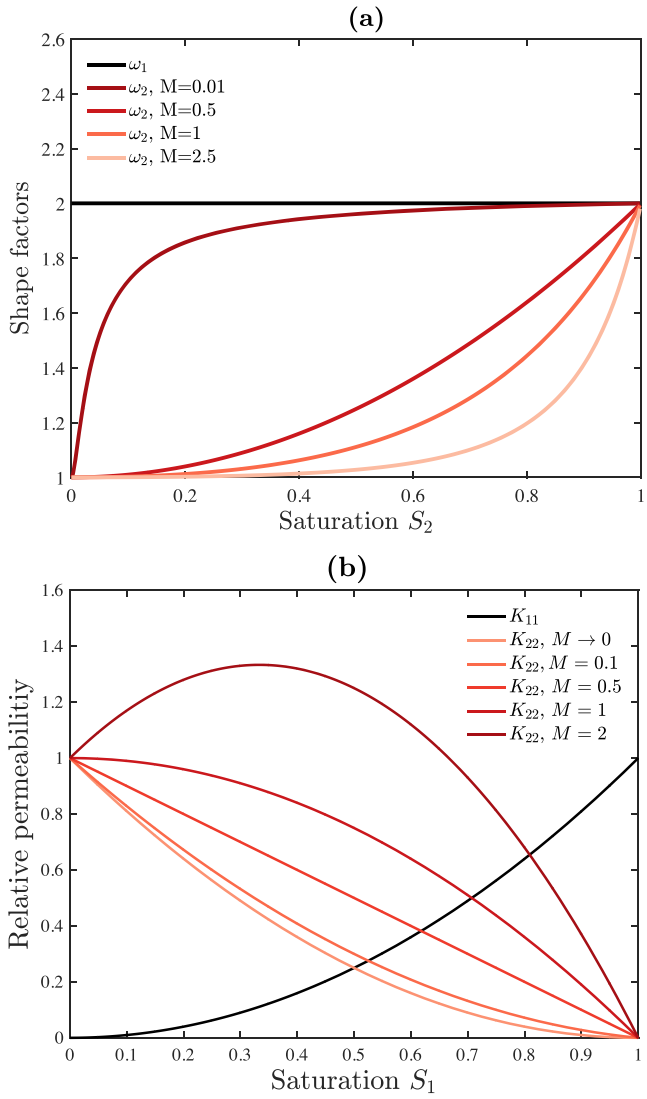


**Figure 5.** (a) Shape factors $\omega_1$ and $\omega_2$ as functions of the saturation of the nonwetting phase $S_2$ and the viscosity ratio $M$ in the limit of a capillary tube of length $L \to 0$. (b) Relative permeabilities of the wetting phase, $K_{11}$, and the nonwetting phase, $K_{22}$, as functions of the saturation of the wetting phase, $S_1$, for core-annular flow in a capillary tube.

the average velocities, Darcy's law is recovered as a particular case. When also the inertia terms are negligible (sufficiently small *Re* and *R*; see Figure 3a), analytical expressions for the relative permeabilities can be derived by rearranging equation (26) as follows

$$\langle \overline{\boldsymbol{u}}_1 \rangle = -\frac{K_{11}}{32}\nabla p_1 \quad \text{with} \quad K_{11} = S_1^2, \tag{31a}$$

$$\langle \overline{\boldsymbol{u}}_2 \rangle = -\frac{K_{22}}{32M}\nabla p_2 \quad \text{with} \quad K_{22} = (2MS_1 - S_1 + 1)(1 - S_1), \tag{31b}$$

$$p_1 - p_2 = \frac{2\varepsilon}{Ca\sqrt{1 - S_1}}, \tag{31c}$$

where the average curvature is $\langle \overline{\kappa} \rangle = 2/\sqrt{1 - S_1}$. Thus, we have obtained a formulation for the relative permeabilities as a result of the postulation of the flow-regime at the pore-scale including both the interaction between the wetting phase and the wall and between the two fluids. Since the two phases have the same pressure gradient, we do not have obtained here any of the coupling terms.

It is worth noticing that $K_{11}$ is independent of the viscosity ratio and $0 < K_{11} < 1$, while $K_{22}$ depends both on the viscosity ratio and the saturation of the wetting phase: when the nonwetting phase (core) is more viscous than the wetting phase (annulus), $K_{22}$ may reach values larger than 1 (see Figure 5b); that is, the flux of the nonwetting phase is greater than the flux of the nonwetting phase in the same geometry at single-phase conditions. This is true only if the nonwetting phase is the most viscous phase ($M > 1$): due to lubrication effects, when the more viscous fluid is not in contact with the wall, the resulting effect is similar to having an effective slip at the solid wall (see Berg et al., 2008). Additionally, equation (31b) shows that $K_{22}$ in a capillary tube is unbounded for $M$ that goes to infinity. In a real porous medium these conditions may be realized only in localized regions (i.e., in proximity of a drop surrounded by a wetting layer of a less viscous fluid) and not over a large portion of the porous matrix. As a result, while theoretically possible, the macroscopic relative permeability of the nonwetting phase in a real porous medium is, often, not greater than 1. Finally, in the limit $M \to 0$, $K_{22} = (1 - S_1)^2$, which matches the relative permeability of the connected pathway flow. Importantly, the previous closures are consistent with the single-phase limit when either one of the phases is absent, in particular, when $S_1 \to 1$, $K_{22} \to 0$, and $K_{11} \to 1$; or when $S_1 \to 0$, $K_{22} \to 1$, and $K_{11} \to 0$.

### 4.4. Plug Flow in a Capillary Tube

The plug flow regime consists in a sequence of taps of a continuous phase and elongated bubbles (or elongated drops in liquid-liquid systems), which are surrounded by a film of the continuous phase (plug region; see Figure 1c). This flow regime has been extensively studied both in large pipes (see Fabre & Line, 1992; Picchi, Manerba, et al., 2015b) and in capillary tubes (see, e.g., Abu-Al-Saud et al., 2017; Jovanovic et al., 2011; Kawahara et al., 2002; Tsaoulidis & Angeli, 2016; Ullmann & Brauner, 2007; Wegmann & von Rohr, 2006; Yagodnitsyna et al., 2016). Plug flow is also intrinsically an intermittent flow regime: since the bubble (or drop) length is not constant (see Hout et al., 1992), we refer to the average length of the elongated bubble; see, for example, the experimental works by Kashid and Agar (2007) and Tsaoulidis and Angeli (2016).

Here we focus on plug flow in a capillary tube of diameter $D$ and length $L$ where the bubble (or drop) is sufficiently long to form a region with a uniform film thickness (see Picchi et al., 2018). Specifically, we assume that the unit cell $Y$ contains an average (representative) plug unit cell, and we model (i) the plug region of length $\ell$ (see Figure 1c) as a (local) region of fully developed core-annular flow and (ii) the single-phase region ($1 - \ell$ in Figure 1c) as single phase flow of the wetting phase. Therefore, equation (18) for the plug flow regime yields

$$\varepsilon Re \mathcal{K}_1 \omega_1 \left\langle \overline{\boldsymbol{u}}_1 \right\rangle_{\mathcal{B}_1}^2 = -\nabla p_1 + 32\ell \left( M \frac{\langle \overline{\boldsymbol{u}}_2 \rangle_{\mathcal{B}_{2P}} - 2\langle \overline{\boldsymbol{u}}_1 \rangle_{\mathcal{B}_{1P}}}{S_{1P}} - \frac{\langle \overline{\boldsymbol{u}}_1 \rangle_{\mathcal{B}_{1P}}}{S_{1P}^2} \right) + 32(1-\ell)\langle \overline{\boldsymbol{u}}_1 \rangle_{\mathcal{B}_{1S}}, \tag{32a}$$

$$\varepsilon R Re \mathcal{K}_2 \omega_2 \left\langle \overline{\boldsymbol{u}}_2 \right\rangle_{\mathcal{B}_2}^2 = -\nabla p_2 + 32M\ell \left( \frac{2\langle \overline{\boldsymbol{u}}_1 \rangle_{\mathcal{B}_{1P}} - \langle \overline{\boldsymbol{u}}_2 \rangle_{\mathcal{B}_{2P}}}{1 - S_{1P}} \right), \tag{32b}$$

$$p_1 - p_2 = \frac{\langle \overline{\kappa} \rangle \varepsilon}{Ca} \quad \text{where} \quad \langle \overline{\kappa} \rangle \sim \ell \frac{1}{\sqrt{1 - S_{1P}}}, \tag{32c}$$

where the subscripts $P$ and $S$ refer to the plug and single-phase regions, respectively. Specifically, $\mathcal{B}_{1\mathbf{P}}$ and $\mathcal{B}_{2\mathbf{P}}$ are the dimensionless volume occupied by the phase 1 and 2 in the plug region, respectively ($\mathcal{B}_{1\mathbf{P}} \cup \mathcal{B}_{1\mathbf{S}} = \mathcal{B}_1$ and $\mathcal{B}_2 = \ell \mathcal{B}_{2\mathbf{P}}$), while $\mathcal{B}_{1\mathbf{S}}$ is the dimensionless volume occupied by the phase 1 in the single phase region. We model the stress terms as core-annular flow in the plug region ($\ell$ in Figure 1) and single phase of the wetting phase in the $(1 - \ell)$ region according to the definition provided in equation (C13) of Appendix C, that is,

$$\mathcal{T}_{f1} = -\ell \langle \overline{\boldsymbol{\tau}}_f \rangle_{\mathcal{B}_{1P}} \frac{\Gamma_{12\mathbf{P}}}{\mathcal{B}_{1\mathbf{P}}}, \quad \text{and} \quad \mathcal{T}_{w1} = \ell \langle \overline{\boldsymbol{\tau}}_w \rangle_{\mathcal{B}_{1\mathbf{P}}} \frac{\Gamma_{1\mathbf{P}}}{\mathcal{B}_{1\mathbf{P}}}, + (1-\ell) \langle \overline{\boldsymbol{\tau}}_w \rangle_{\mathcal{B}_{1\mathbf{S}}} \frac{\Gamma_{1\mathbf{S}}}{\mathcal{B}_{1S}}, \tag{33a}$$

$$\mathcal{T}_{f2} = \ell \langle \overline{\boldsymbol{\tau}}_f \rangle_{\mathcal{B}_{2\mathbf{P}}} \frac{\Gamma_{12\mathbf{P}}}{\mathcal{B}_{2\mathbf{P}}}, \quad \text{and} \quad \mathcal{T}_{w2} = 0. \tag{33b}$$

The saturation of the wetting phase over the unit cell is given by

$$S_1 = \ell S_{1\mathbf{P}} + 1 - \ell, \tag{34}$$

where $S_{1\mathbf{P}}$ is the saturation of the wetting phase within the plug region, and it is related to the thickness of the annulus surrounding the bubble, namely, the film thickness $h$, by the following relation

$$h = 1 - \sqrt{1 - S_{1\mathbf{P}}}. \tag{35}$$

Note that the film thickness $h$ is the only free parameter of the problem and can be determined, for example, by experiments (see, e.g., Roumpea et al., 2017) or by theory-based correlations (see Bretherton, 1961; Hodges et al., 2004; Picchi et al., 2018), where the film thickness is expressed as a function of the capillary number and the dimensionless parameters of the system, $h = h(Ca, M, \ldots)$. The problem then is closed with the following relation between the average velocities:

$$\langle \overline{\boldsymbol{u}}_1 \rangle_{B_1} = \ell \langle \overline{\boldsymbol{u}}_1 \rangle_{B_{1\mathrm{P}}} + (1-\ell)\langle \overline{\boldsymbol{u}}_1 \rangle_{B_{1\mathrm{S}}}, \tag{36a}$$

$$\langle \overline{\boldsymbol{u}}_2 \rangle_{B_2} = \ell \langle \overline{\boldsymbol{u}}_2 \rangle_{B_{2\mathrm{P}}}, \tag{36b}$$

where $\langle \overline{\boldsymbol{u}}_1 \rangle_{B_{1\mathrm{S}}}$ is the average velocity in the single-phase region, $(1-\ell)$, equal to the mixture velocity (Fabre & Line, 1992; Picchi et al., 2018) as

$$\langle \overline{\boldsymbol{u}}_1 \rangle_{B_{1\mathrm{S}}} = S_{1\mathrm{P}} \langle \overline{\boldsymbol{u}}_1 \rangle_{B_{1\mathrm{P}}} + (1-S_{1\mathrm{P}})\langle \overline{\boldsymbol{u}}_2 \rangle_{B_{2\mathrm{P}}}. \tag{37}$$

Under the assumption that inertia terms (LHS of equation (32)) are negligible and the macroscopic pressure gradient is the same for both phases, we recover the two-phase Darcy's law and analytical expressions for the relative permeabilities:

$$\left\langle \overline{\boldsymbol{u}}_1 \right\rangle = -\frac{K_{11}}{32}\nabla p_1, \tag{38a}$$

$$\left\langle \overline{\boldsymbol{u}}_2 \right\rangle = -\frac{K_{22}}{32M}\nabla p_2, \tag{38b}$$

$$K_{11} = \frac{\left[(1-M)\,S_{1\mathrm{P}} - S_{1\mathrm{P}}^3 + S_{1\mathrm{P}}^2\right] S_1 + S_{1\mathrm{P}}\left(S_{1\mathrm{P}}-1\right)\left(S_{1\mathrm{P}}^2 + M - 1\right)}{M\left[S_1\left(1 + S_{1\mathrm{P}} - S_{1\mathrm{P}}^2\right) + S_{1\mathrm{P}}^3 - S_{1\mathrm{P}}^2 - S_{1\mathrm{P}} - 1\right]} S_1 \tag{38c}$$

$$K_{22} = \frac{\left[S_{1\mathrm{P}}^4 - S_{1\mathrm{P}}^3 + (2M-1)\,S_{1\mathrm{P}} + 1\right] - S_{1\mathrm{P}}^5 + S_{1\mathrm{P}}^4 + (1-2M)S_{1\mathrm{P}} - 1}{\left(1-S_{1\mathrm{P}}\right)\left(S_{1\mathrm{P}}^2 - S_{1\mathrm{P}} - 1\right)S_1 + \left(S_{1\mathrm{P}}-1\right)\left(S_{1\mathrm{P}}^3 - S_{1\mathrm{P}}^2 - S_{1\mathrm{P}} - 1\right)}(S_1 - 1). \tag{38d}$$

Note that the relative permeabilities, $K_{11}(S_1, S_{1\mathrm{P}}, M)$ and $K_{22}(S_1, S_{1\mathrm{P}}, M)$, plotted in Figure 6, depend only on the unit cell saturation, $S_1$, the saturation in the plug region $S_{1\mathrm{P}}$ (i.e., the film thickness $h$; see equation (35)), and the viscosity ratio $M$. Furthermore, the structure of the relative permeabilities is consistent with the one obtained for the core-annular flow regime: when $M > \sim 0.4$, the relative permeability curve of the nonwetting phase, $K_{22}$, for the core-annular flow regime represents an upper bound for the relative permeability of plug flow at a fixed saturation (see Figures 6). However, the trend is opposite for $M <\sim 0.4$, where the wetting phase flux is higher for the plug flow regimes, as expected. In other words, at a fixed saturation, $K_{22}$ for the plug flow regime is bounded by the one for core-annular flow. Moreover, for sufficiently low viscosity ratios, $M <\sim 0.4$, increasing the film thickness yields to a lower relative permeability of the nonwetting phase, while the behavior is opposite for $M > \sim 0.4$.

It is worth highlighting the expected behavior (i) in the limit of thin film surrounding the bubble, $h \to 0$ and $S_{1\mathrm{P}} \to 0$, where one obtains $K_{11} = S_1^2/M(1-S_1)$ and $K_{22} = (1-S_1)$, and (ii) in the limit of vanishing nonwetting phase, where $K_{11} \to 1$ for both $S_1 \to 1$ and $S_{1\mathrm{P}} \to 1$, consistently to the single-phase case. In addition, conditions where the relative permeability of the nonwetting phase reaches values bigger than unity are theoretically possible also for the plug flow regime (see Figure 6).

### 4.5. Impact of Flow Regimes on the Relative Permeability

In many applications it is of interest to quantify how much of the nonwetting phase can be transported through the porous matrix, and based on our previous analysis, we have shown that the flux (i.e., the average velocity) of the nonwetting phase is strongly affected by the flow regimes at the pore scale. Here, we investigate the impact of pore-scale flow regimes on the relative permeability curves. Specifically, we compute, at a fixed saturation, the relative error between the relative permeability for core-annular flow and those in the plug flow and connected pathway regimes, that is,

$$e_{K_{22}} = \frac{|K_{22,\mathrm{PLUG}} - K_{22,\mathrm{CAF}}|}{K_{22,\mathrm{CAF}}}, \qquad e_{K_{22,\mathrm{CP}}} = \frac{|K_{22,\mathrm{CP}} - K_{22,\mathrm{CAF}}|}{K_{22,\mathrm{CAF}}}, \tag{39}$$

where $K_{22,\mathrm{CAF}}$, $K_{22,\mathrm{PLUG}}$, and $K_{22,\mathrm{CP}}$ are the relative permeabilities of the nonwetting phase for core-annular flow (CAF), plug flow (PLUG), and connected pathway (CP) flow regimes given by equations (31b), (38d), and (25b),

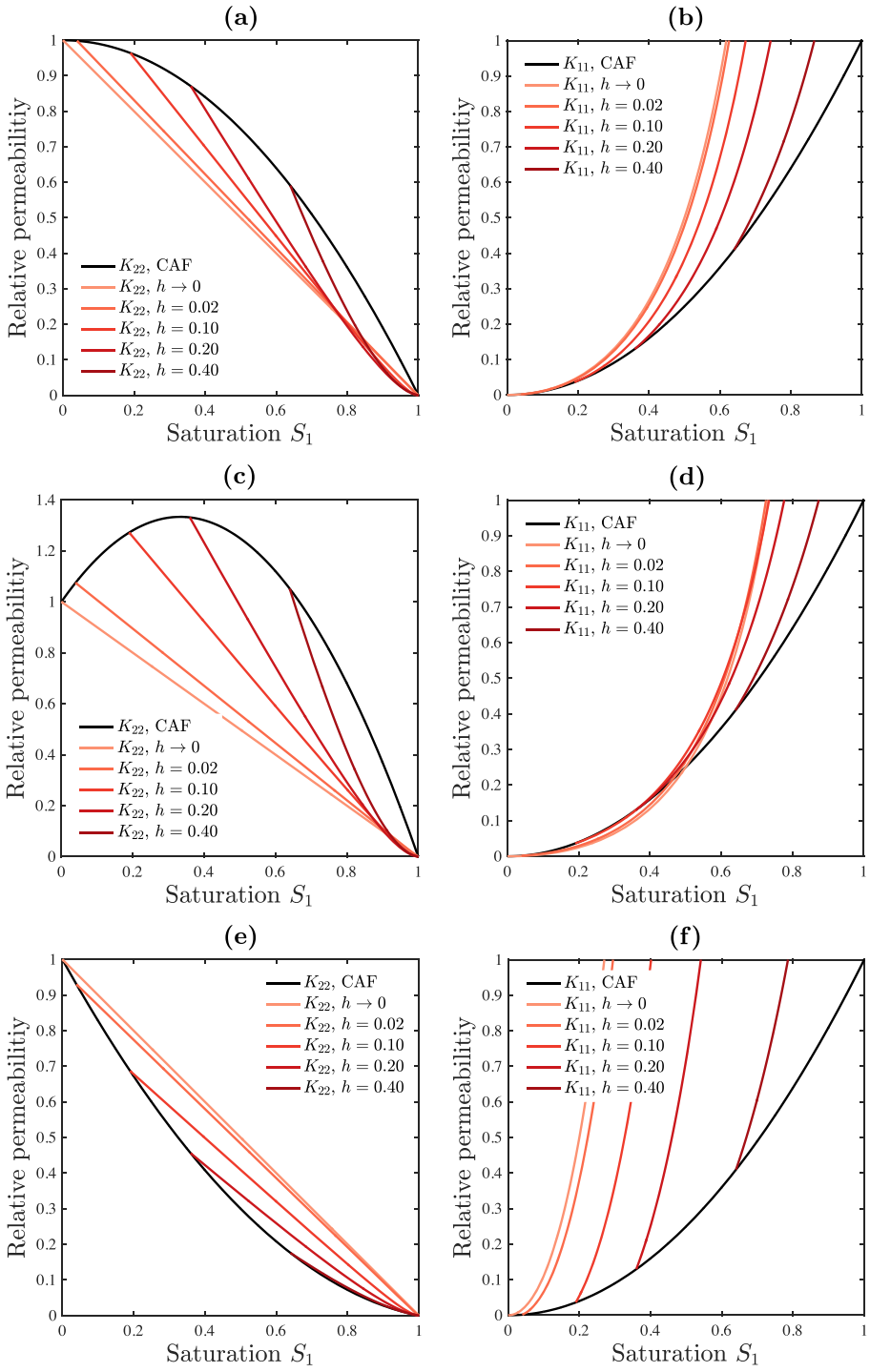


**Figure 6.** Relative permeabilities of the wetting phase, $K_{11}$, and the nonwetting phase, $K_{22}$, as functions of the saturation of the wetting phase, $S_1$, and the film thickness surrounding the bubble, $h$, for plug flow in a capillary tube for the case of $M = 1$ (a, b), $M = 2$ (c, d), and $M = 0.1$ (e, f). CAF refers to core-annular flow.

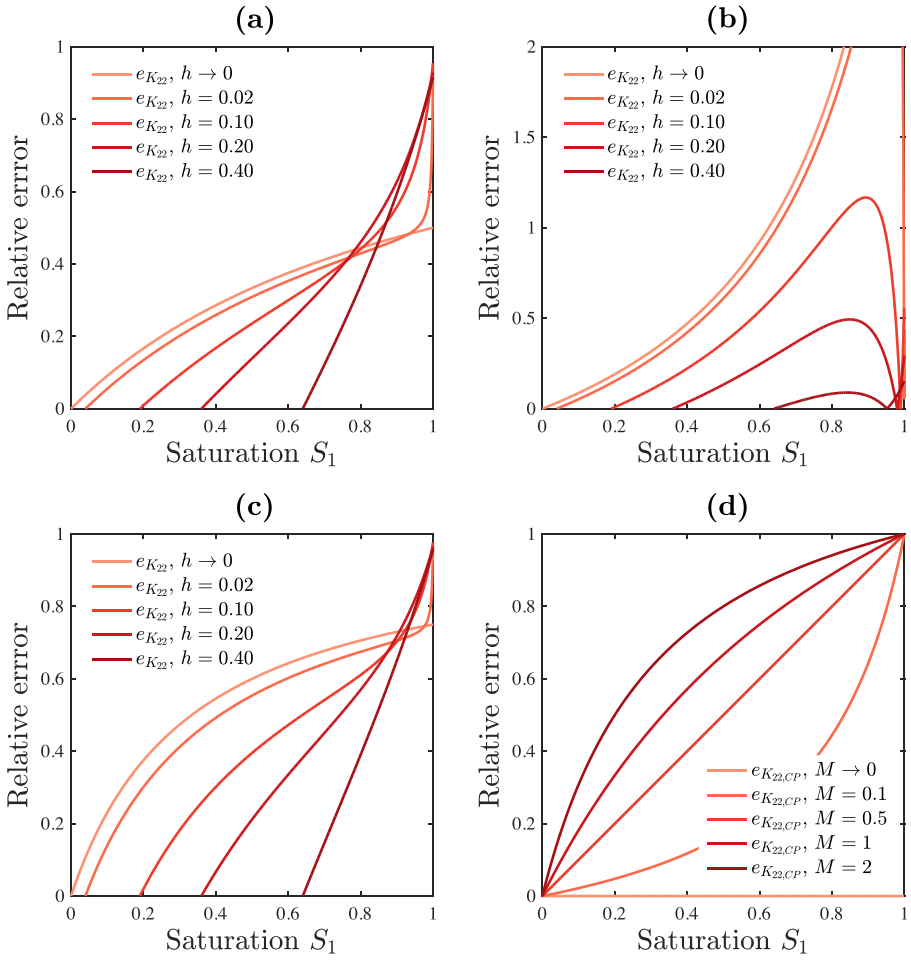


**Figure 7.** Relative error between the relative permeability of the nonwetting phase, $K_{22}$, for the plug flow compared to the core annular-flow as a function of the saturation of the wetting phase, $S_1$, and the film thickness surrounding the bubble, $h$, for (a) $M = 1$, (b) $M = 0.1$, and (c) $M = 2$. (d) Relative error for the connected pathway flow compared to the core annular flow as a function of the saturation of the wetting phase, $S_1$, and the viscosity ratio of the system, $M$ .

respectively. The trends of the relative error of the plug flow, $e_{K_{22}}$, are presented in Figure 7 as a function of the saturation and the viscosity ratio. In case of iso-viscous fluid, that is, $M = 1$, the error is still considerable (up to 40%) for low saturation of the wetting phase, and it reaches a value close to 100% at higher saturations. For a very thin film of the wetting phase surrounding the bubble, $h \to 0$, we obtain that, at low saturation, the difference between the core-annular and plug flow relative permeability curves is maximal. The discrepancy increases with an increase of the viscosity ratio. Furthermore, for systems characterized by low viscosity ratios ($M = 0.1$, case (b) Figure 7), differences in the predicted relative permeability is considerable in the whole range of saturation, and it reaches a peak larger than 100% at high saturations. The case of a very thin film is also in this case the worst scenario.

By inspection of the discrepancies between the relative permeability for the core-annular and for the connected pathway flow regime, we see that the error is almost 0 when the viscosity ratio is sufficiently small, as shown in Figure 7d ($e_{K_{22,CP}}$ approaches 0 for $M \to 0$). Therefore, if the wetting phase is much more viscous than the nonwetting phase such as for water-steam or air-water systems, the predicted relative permeability will be the same both for connected pathway and core annular flow. Otherwise, the error is considerable in the whole range of saturations at viscosity ratios close to or larger than 1.

From the analysis of the relative errors, we can conclude that the impact of pore-scale flow regimes on relative permeabilities is significant. In fact, not properly accounting for the phase topology at the pore scale may lead to severe mispredictions of the relative permeability and, as a consequence, of the filtration velocity.

## 5. Conclusions

Recent experimental and numerical results (see Armstrong et al., 2016; Avraam & Payatakes, 1995a) have identified four possible pore-scale flow regimes (i.e., large-ganglion dynamics, small-ganglion dynamics, drop traffic flow, and connected-pathway flow) which strongly affect the macroscopic filtration velocity. Since the penetration of existing upscaled models, such as the methods which account for the evolution of fluid-fluid interface (e.g., Gray et al., 2015; Gray & Miller, 2010; Hilfer, 1998; Jackson et al., 2009; Niessner & Hassanizadeh, 2008), has been hindered by the difficulties of their parametrization, in this work, we have investigated the impact of pore-scale flow regimes, that is, the topology of flowing phases, on the upscaled equations for two-phase flow in porous media. Specifically, we propose a homogenization framework that allows one to derive upscaled equations that are regime specific. We aim at incorporating the interactions between the flowing phases and the solid while retaining simplicity of the final formulation.

To achieve such a goal, we formulate the pore-scale problem (Navier-Stokes equations) of two incompressible fluids in a porous medium, we identify the relevant dimensionless parameters, and we derive a new set of macroscopic equations by means of multiple-scale expansions. Differently from previous works, we proceed by postulating the pore-scale flow regimes and by proposing an analogy between such flow regimes in a real porous medium and two-phase flow in a capillary tube. Using this analog, we analytically determine the effective parameters of the upscaled equation. Specifically, we model the connected-pathway flow as a bundle of capillary tubes, while large-ganglion dynamics and small-ganglion dynamics have been modeled in analogy with the core-annular flow and the plug flow in a capillary tube. This approach allows us to reduce the complexity due to the geometry of the flowing phases and, at the same time, to retain the physics behind the interaction between the phases. In addition, we show that our approach reduces to the two-phase Darcy's law as a particular case, where we obtained analytical expressions for the relative permeability of the wetting and the nonwetting phase for each flow regime (i.e., connected pathway, core-annular flow, and plug flow).

Our analysis leads to the following major conclusions:

1. We propose regime-specific upscaled equations for the basic pore-scale flow regimes. Their effective parameters are determined while accounting for the phase topology. The relative permeabilities for the connected pathway flow regime depend only on the saturation, while the ones for the core-annular flow depend also on the viscosity ratio. Modeling of the plug flow requires one additional closing parameter, namely, the film thickness which surrounds the bubble (or drop) at the pore scale.
2. We show that the lack of two-phase model predictive capabilities is accentuated when flow regimes are not taken into account: differences in the relative permeability between the core-annular flow and the plug flow regimes at a fixed saturation may be significant. In fact, not accounting for the pore-scale flow regimes can lead to severe mispredictions of filtration velocity in the multiphase flow context.
3. We also investigate the applicability conditions for the proposed upscaled equations in terms of phase diagrams based on the order of magnitude of relevant dimensionless numbers (i.e., Reynolds, capillary, Froude numbers, and the viscosity and density ratio). Interestingly, we obtained that the capillary number alone is not sufficient to classify the system, but the average pore-scale curvature plays a significant role. In particular, the inequality of the macroscopic pressure is recovered only if the ratio of the capillary number and the pore-scale average curvature is within a specific range. We also investigated the limitations of the classical two-phase Darcy's law.

Notwithstanding the simplicity of the configuration investigated (flow in a capillary tube), this analysis provides a framework to quantify the importance of topology of the flowing phases on relative permeability estimates. Generalization of the proposed analytical expressions linking pore-scale topology of the flowing phases and their viscosity ratios with relative permeability and saturation to real porous media is subject of current investigations.

## Appendix A: Multiple-Scale Expansions of Navier-Stokes Equations

Replacing the expanded variables (equation (11)) and the dimensionless numbers (equation (13)) into the Navier-Stokes equations (equations (5b) and (5c)) and substituting the following relations for the spatial differential operators

$$\nabla = \nabla_x + \varepsilon^{-1}\nabla_y\,,$$
$$\nabla\cdot = \nabla_x\cdot + \varepsilon^{-1}\nabla_y\cdot\,,$$
$$\nabla^2 = \nabla_x^2 + \varepsilon^{-2}\nabla_y^2 + 2\varepsilon^{-1}\left(\nabla_x\cdot\nabla_y\right)\,, \tag{A1}$$

we obtain

$$\begin{aligned}&\varepsilon^{1+\alpha}\frac{\partial\left(\boldsymbol{u}_1^{(0)}+\varepsilon\boldsymbol{u}_1^{(1)}\right)}{\partial s} + \varepsilon^{2+\alpha}\left(\boldsymbol{u}_1^{(0)}+\varepsilon\boldsymbol{u}_1^{(1)}\right)\cdot\left(\nabla_x+\frac{1}{\varepsilon}\nabla_y\right)\left(\boldsymbol{u}_1^{(0)}+\varepsilon\boldsymbol{u}_1^{(1)}\right) =\\ &-\nabla_x\left(p_1^{(0)}+\varepsilon p_1^{(1)}\right) - \frac{1}{\varepsilon}\nabla_y\left(p_1^{(0)}+\varepsilon p_1^{(1)}\right) + \varepsilon^2\nabla_x^2\left(\boldsymbol{u}_1^{(0)}+\varepsilon\boldsymbol{u}_1^{(1)}\right) + \nabla_y^2\left(\boldsymbol{u}_1^{(0)}+\varepsilon\boldsymbol{u}_1^{(1)}\right)\\ &+2\varepsilon\left(\nabla_x\cdot\nabla_y\right)\left(\boldsymbol{u}_1^{(0)}+\varepsilon\boldsymbol{u}_1^{(1)}\right) + \varepsilon^{2+\alpha-2\beta}\boldsymbol{e_g} = 0,\end{aligned} \tag{A2a}$$

$$\begin{aligned}&\varepsilon^{1+\gamma+\alpha}\frac{\partial\left(\boldsymbol{u}_2^{(0)}+\varepsilon\boldsymbol{u}_2^{(1)}\right)}{\partial s} + \varepsilon^{2+\gamma+\alpha}\left(\boldsymbol{u}_2^{(0)}+\varepsilon\boldsymbol{u}_2^{(1)}\right)\cdot\left(\nabla_x+\frac{1}{\varepsilon}\nabla_y\right)\left(\boldsymbol{u}_2^{(0)}+\varepsilon\boldsymbol{u}_2^{(1)}\right) =\\ &-\nabla_x\left(p_2^{(0)}+\varepsilon p_2^{(1)}\right) - \frac{1}{\varepsilon}\nabla_y\left(p_2^{(0)}+\varepsilon p_2^{(1)}\right) + \varepsilon^{2+\delta}\nabla_x^2\left(\boldsymbol{u}_2^{(0)}+\varepsilon\boldsymbol{u}_2^{(1)}\right) + \varepsilon^{\delta}\nabla_y^2\left(\boldsymbol{u}_2^{(0)}+\varepsilon\boldsymbol{u}_2^{(1)}\right)\\ &+2\varepsilon^{1+\delta}\left(\nabla_x\cdot\nabla_y\right)\left(\boldsymbol{u}_2^{(0)}+\varepsilon\boldsymbol{u}_2^{(1)}\right) + \varepsilon^{2+\gamma+\alpha-2\beta}\boldsymbol{e_g} = 0.\end{aligned} \tag{A2b}$$

Similarly, the expanded continuity equations (equation (5a) yield

$$\nabla_x\cdot\left(\boldsymbol{u}_1^{(0)}+\varepsilon\boldsymbol{u}_1^{(1)}\right) + \frac{1}{\varepsilon}\nabla_y\cdot\left(\boldsymbol{u}_1^{(0)}+\varepsilon\boldsymbol{u}_1^{(1)}\right) = 0, \tag{A3a}$$

$$\nabla_x\cdot\left(\boldsymbol{u}_2^{(0)}+\varepsilon\boldsymbol{u}_2^{(1)}\right) + \frac{1}{\varepsilon}\nabla_y\cdot\left(\boldsymbol{u}_2^{(0)}+\varepsilon\boldsymbol{u}_2^{(1)}\right) = 0. \tag{A3b}$$

Expanding the normal and tangential shear stress continuity boundary condition at the fluid-fluid interface (equations (7d) and (7e)), we obtain

$$\begin{aligned}&\left(p_1^{(0)}+\varepsilon p_1^{(1)}-p_2^{(0)}+\varepsilon p_2^{(1)}\right)\boldsymbol{I} + \varepsilon^2\boldsymbol{n}\cdot\left[\nabla_x\left(\boldsymbol{u}_1^{(0)}+\varepsilon\boldsymbol{u}_1^{(1)}\right) + \frac{1}{\varepsilon}\nabla_y\left(\boldsymbol{u}_1^{(0)}+\varepsilon\boldsymbol{u}_1^{(1)}\right)\right.\\ &+\nabla_x\left(\boldsymbol{u}_1^{(0)}+\varepsilon\boldsymbol{u}_1^{(1)}\right)^T + \frac{1}{\varepsilon}\nabla_y\left(\boldsymbol{u}_1^{(0)}+\varepsilon\boldsymbol{u}_1^{(1)}\right)^T - \varepsilon^{\delta}\nabla_x\left(\boldsymbol{u}_2^{(0)}+\varepsilon\boldsymbol{u}_2^{(1)}\right) - \varepsilon^{\delta-1}\nabla_y\left(\boldsymbol{u}_2^{(0)}+\varepsilon\boldsymbol{u}_2^{(0)}\right)\\ &\left.-\varepsilon^{\delta}\nabla_x\left(\boldsymbol{u}_2^{(0)}+\varepsilon\boldsymbol{u}_2^{(1)}\right)^T - \varepsilon^{\delta-1}\nabla_y\left(\boldsymbol{u}_2^{(0)}+\varepsilon\boldsymbol{u}_2^{(1)}\right)^T\right]\cdot\boldsymbol{n} = -\varepsilon^{1-\eta+\theta}\left(\kappa_1^{(0)}+\varepsilon\kappa_1^{(1)}\right) \quad \text{on} \quad \Gamma_{12},\end{aligned} \tag{A4}$$

$$\begin{aligned}&\boldsymbol{t}\cdot\left[\nabla_x\left(\boldsymbol{u}_1^{(0)}+\varepsilon\boldsymbol{u}_1^{(1)}\right) + \frac{1}{\varepsilon}\nabla_y\left(\boldsymbol{u}_1^{(0)}+\varepsilon\boldsymbol{u}_1^{(1)}\right) + \nabla_x\left(\boldsymbol{u}_1^{0}+\varepsilon\boldsymbol{u}_1^{(1)}\right)^T + \frac{1}{\varepsilon}\nabla_y\left(\boldsymbol{u}_1^{0}+\varepsilon\boldsymbol{u}_1^{(1)}\right)^T\right.\\ &-\varepsilon^{\delta}\nabla_x\left(\boldsymbol{u}_2^{(0)}+\varepsilon\boldsymbol{u}_2^{(1)}\right) - \varepsilon^{\delta-1}\nabla_y\left(\boldsymbol{u}_2^{(0)}+\varepsilon\boldsymbol{u}_2^{(1)}\right) - \varepsilon^{\delta}\nabla_x\left(\boldsymbol{u}_2^{(0)}+\varepsilon\boldsymbol{u}_2^{(1)}\right)^T\\ &\left.-\varepsilon^{\delta-1}\nabla_y\left(\boldsymbol{u}_2^{(0)}+\varepsilon\boldsymbol{u}_2^{(1)}\right)^T\right]\cdot\boldsymbol{n} = 0 \quad \text{on} \quad \Gamma_{12}.\end{aligned} \tag{A5}$$

## Appendix B: Reformulation of the Derivation of the Two-Phase Darcy's Law

The two-phase Darcy's law is obtained by homogenization via multiple-scale expansions of the Stokes equations for both phases, namely, neglecting time derivatives and inertia terms in the Navier-Stokes equations. Equation (5) is expanded, as shown in Appendix A, while imposing that $\alpha > -1$ and $\alpha + \gamma < -1$. Collecting terms of like-powers of $\varepsilon$ ($\varepsilon^{-1}$) in equations (A2a) and (A2b), at the leading order we obtain

$$\nabla_y p_1^{(0)} = 0, \quad \boldsymbol{x},\boldsymbol{y}\in\mathcal{B}_1 \quad \text{and} \quad \nabla_y p_2^{(0)} = 0, \quad \boldsymbol{x},\boldsymbol{y}\in\mathcal{B}_2, \tag{B1}$$

i.e., $p_1^{(0)}$ and $p_2^{(0)}$ the macroscopic pressures depend only on the slow space variable $\boldsymbol{x}$; we assume that both the macroscopic pressures do not depend on the fast time variable $s$. We proceed by collecting the leading order in the expanded normal shear stress boundary condition (equation (A4)), and recover a relation between the macroscopic pressures

$$p_1^{(0)} - p_2^{(0)} = \kappa_1^{(0)} \quad \text{on} \quad \Gamma_{12}, \tag{B2}$$

only when $1-\eta+\theta=0$. This requirement constrains the local pore-scale curvature and the capillary number, specifically $O(\kappa/Ca)=\varepsilon^{-1}$). If $1-\eta+\theta>0$, the analysis gives us the equality of the macroscopic pressures, $p_1^{(0)}=p_2^{(0)}$. On the other hand, we obtain that the scales are coupled for $1-\eta+\theta<0$; that is, the problem cannot be homogenized under these conditions.

Collecting the terms of order $\varepsilon^0$ in equations (A2a)–(A3b) we obtain

$$\nabla_y\cdot\boldsymbol{u}_i^{(0)}=0,\qquad \boldsymbol{x},\boldsymbol{y}\in\mathcal{B}_i,\quad i=1,2 \tag{B3}$$

and

$$-\nabla_x p_1^{(0)}-\nabla_y p_1^{(1)}+\nabla_y^2\boldsymbol{u}_1^{(0)}+\varepsilon^{2+\alpha-2\beta}\boldsymbol{e_g}=0,\qquad \boldsymbol{x},\boldsymbol{y}\in\mathcal{B}_1, \tag{B4a}$$

$$-\nabla_x p_2^{(0)}-\nabla_y p_2^{(1)}+\varepsilon^{\delta}\nabla_y^2\boldsymbol{u}_2^{(0)}+\varepsilon^{2+\gamma+\alpha-2\beta}\boldsymbol{e}_g=0,\qquad \boldsymbol{x},\boldsymbol{y}\in\mathcal{B}_2. \tag{B4b}$$

By analysis of the order of magnitude of the terms of equations (B4a) and (B4b), we observe that for $\delta>0$, the viscous terms of phase 2 disappears from equation (B4b) jumping to lower-order equations, while for $\delta<0$, the scales are coupled since the viscous term jumps into the higher (leading) order. Therefore, only if $\delta=0$, that is, the viscosity ratio is a term of order 1, we recover the same structure of Stokes equation with two external driving forces (the gravitational body force and the macroscopic pressure gradient), similarly to the *two-pressure Stokes problem* defined during the homogenization of single-phase flow (see Auriault & Adler, 1995). In a large number of applications the viscosity of the two fluids is comparable, except in the context of very viscous and heavy oil or geothermal reservoir, where the viscosity difference between the liquid water and the steam can be considerable depending on temperature and pressure conditions. We also obtain that the gravitational body force should be accounted only for $2+\alpha-2\beta=0$ and $2+\gamma+\alpha-2\beta=0$ , while it can be neglected (microgravity conditions) in case $2+\alpha-2\beta>0$ and $2+\gamma+\alpha-2\beta>0$.

The boundary conditions for the $\varepsilon^0$ order problem yield

$$\left(p_1^{(1)}-p_2^{(1)}\right)\boldsymbol{I}+\boldsymbol{n}\cdot\left[\nabla_y\boldsymbol{u}_1^{(0)}+\nabla_y\boldsymbol{u}_1^{(0)^T}-\varepsilon^{\delta}\left(\nabla_y\boldsymbol{u}_2^{0}+\nabla_y\boldsymbol{u}_2^{(0)^T}\right)\right]\cdot\boldsymbol{n}=\kappa_1^{(1)}\quad\text{on}\quad\Gamma_{12}, \tag{B5a}$$

$$\boldsymbol{t}\cdot\left[\nabla_y\boldsymbol{u}_1^{(0)}+\nabla_y\boldsymbol{u}_1^{(0)^T}-\varepsilon^{\delta}\left(\nabla_y\boldsymbol{u}_2^{(0)}+\nabla_y\boldsymbol{u}_2^{(0)^T}\right)\right]\cdot\boldsymbol{n}=0\quad\text{on}\quad\Gamma_{12}, \tag{B5b}$$

$$\boldsymbol{u}_i^{(0)}=0\quad\text{and}\quad\boldsymbol{u}_i^{(0)}\cdot\boldsymbol{n}=0\quad\text{on}\quad\Gamma_i, \tag{B5c}$$

$$\boldsymbol{u}_1^{(0)}=\boldsymbol{u}_2^{(0)}\quad\text{on}\quad\Gamma_{12}, \tag{B5d}$$

where $i=1,2$ refers to phase 1 and 2, respectively. Note that the viscous terms in both the continuity of normal and tangential shear stresses (equations (B5a) and (B5b)) are controlled by the magnitude of $\delta$. In the following sections we will formally derive the upscaled equations and the closure problem for the two-phase case.

### B1. Formulation of the Closure Problem: Definition of the Permeability Tensors

The problem at the order $\varepsilon^0$ allows us to formulate the closure problem. In fact, since equation (B4a) is linear and well posed (see Auriault, 1987), it admits a solution of the type

$$\boldsymbol{u}_i^{(0)}=-\boldsymbol{k}_{i1}\nabla_x p_1^{(0)}-\boldsymbol{k}_{i2}\nabla_x p_2^{(0)},\quad \boldsymbol{x},\boldsymbol{y}\in\mathcal{B}_i,\quad i=1,2, \tag{B6}$$

and by analogy

$$\boldsymbol{p}_i^{(1)}=-\boldsymbol{a}_{i1}\nabla_x p_1^{(0)}-\boldsymbol{a}_{i2}\nabla_x p_2^{(0)}+\bar{p}_i,\quad \boldsymbol{x},\boldsymbol{y}\in\mathcal{B}_i,\quad i=1,2, \tag{B7}$$

with $\langle\boldsymbol{a}_{ij}\rangle=0$. Substituting these relations into equations (B4a) and (B4b), while assuming microgravity conditions, we collect the macroscopic pressure gradients and obtain the following local (unit-cell) problems for the closure variables $\boldsymbol{k}_{ij}(\boldsymbol{y})$:

$$\begin{cases}\nabla_y^2\boldsymbol{k}_{11}+\boldsymbol{I}-\nabla_y\mathbf{a}_{11}=0\\ \nabla_y^2\boldsymbol{k}_{12}-\nabla_y\mathbf{a}_{12}=0\end{cases}\quad\begin{cases}\nabla_y\cdot\boldsymbol{k}_{11}=0\\ \nabla_y\cdot\boldsymbol{k}_{12}=0\end{cases}\qquad\boldsymbol{y}\in\mathcal{B}_1, \tag{B8a}$$

$$\begin{cases}\nabla_y^2\boldsymbol{k}_{22}+\boldsymbol{I}-\nabla_y\mathbf{a}_{21}=0\\ \nabla_y^2\boldsymbol{k}_{21}-\nabla_y\mathbf{a}_{21}=0\end{cases}\quad\begin{cases}\nabla_y\cdot\boldsymbol{k}_{21}=0\\ \nabla_y\cdot\boldsymbol{k}_{22}=0\end{cases}\qquad\boldsymbol{y}\in\mathcal{B}_2, \tag{B8b}$$

subjected to the $\varepsilon^0$ order boundary conditions (equations (B5a)–(B5d)). Thus, $\boldsymbol{k}_{ij}(\boldsymbol{y})$ is the solution of the local problem whose uniqueness has been demonstrated by Auriault (1987).

### B2. The Upscaled Equations

The two-phase Darcy's law is recovered by averaging equation (B6) over the unit cell $Y$:

$$\langle \boldsymbol{u}_i \rangle = -\mathbf{K}_{ii}\nabla_x p_1 - \mathbf{K}_{i2}\nabla_x p_2, \qquad \boldsymbol{x} \in \Omega, \quad i = 1, 2, \tag{B9}$$

where $p_i = \langle p_i^{(0)} \rangle$ is the macroscopic pressure. The permeability tensors are obtained by averaging the closure variables, that is, $\mathbf{K}_{ij} = \langle \boldsymbol{k}_{ij} \rangle$. In particular, $\mathbf{K}_{11}$ and $\mathbf{K}_{22}$ are symmetrical, while the role of the viscous coupling tensors $\mathbf{K}_{12}$ and $\mathbf{K}_{21}$ have been widely debated in the literature (see, e.g., Avraam & Payatakes, 1995b; Ayub & Bentsen, 1999).

Finally, a conservation law for the phase saturation is obtained collecting the $\varepsilon^0$ order terms in the continuity equations of the $i$th phase (equations (A3a) and (A3b)) and averaging over the unit cell $Y$, obtaining

$$\frac{1}{|Y|}\int_{\mathcal{B}_i} \nabla_x \cdot \boldsymbol{u}_i^{(0)} \mathrm{d}\boldsymbol{y} + \frac{1}{|Y|}\int_{\mathcal{B}_i} \nabla_y \cdot \boldsymbol{u}_i^{(1)} \mathrm{d}\boldsymbol{y} = 0, \qquad \boldsymbol{x}, \boldsymbol{y} \in \Omega, \quad i = 1, 2. \tag{B10}$$

Then, using Stokes theorem and assuming that the interface $\Gamma_{12}$ is moving very slowly compared to both fluids, we finally obtain a conservation law for the phase saturation (Auriault, 1987),

$$\nabla_x \cdot \langle \boldsymbol{u}_i \rangle + \underbrace{\frac{1}{|Y|}\int_{\Gamma_{12}} \boldsymbol{u}_i^{(1)} \cdot \boldsymbol{n}\, \mathrm{d}\boldsymbol{y}}_{\phi \partial S_i/\partial t} + \underbrace{\frac{1}{|Y|}\int_{\Gamma_i} \boldsymbol{u}_i^{(1)} \cdot \boldsymbol{n} \mathrm{d}\boldsymbol{y}}_{=0 \text{ no-slip}} = 0, \qquad \boldsymbol{x}, \boldsymbol{y} \in \Omega, \quad i = 1, 2. \tag{B11}$$

## Appendix C: Homogenization of the two-phase Navier-Stokes equations

In this appendix, we present the derivation of the new set of upscaled equations obtained by homogenizing the Navier-Stokes equations via multiple scales expansions. Our derivation starts from the Navier-Stokes equation for both phases (equation (5)) and the boundary conditions (equation (7)), where the unsteady and the inertia terms are not a priori neglected. First, we expand equation (5) (see section 3), and obtain (A2a) and (A2b). Then, we proceed by collecting the terms at the same order.

Collecting the terms of the leading order in equations (A2a) and (A2b) and in the boundary condition, equation (A4), we obtain

$$\nabla_y p_1^{(0)} = 0, \quad \boldsymbol{x}, \boldsymbol{y} \in \mathcal{B}_1 \quad \text{and} \quad \nabla_y p_2^{(0)} = 0, \quad \boldsymbol{x}, \boldsymbol{y} \in \mathcal{B}_2, \tag{C1}$$

$$p_1^{(0)} - p_2^{(0)} = \varepsilon^{1-\eta+\theta}\kappa_1^{(0)} \quad \text{on} \quad \Gamma_{12}. \tag{C2}$$

As a consequence, $p_1^{(0)}$ and $p_2^{(0)}$ are the macroscopic pressures which depend only on the slow space variable $\boldsymbol{x}$ since we assume both the macroscopic pressures do not depend on the fast time variable $s$. Differently from the homogenization of the Stokes equations (Appendix B), we are able to relax some of the scale separation constraints: the scale separation is guaranteed when $\alpha \leq -1$, $Re \leq 1/\varepsilon$, and $\alpha + \gamma \leq -1$, $Re \cdot R \leq 1/\varepsilon$, while the relation between the macroscopic pressure hold for $1 - \eta + \theta \geq 0$.

Next, we collect terms of order $\varepsilon^0$ in equations (A2a)–(A2b), and we look at the general case where the time derivative, the inertia, and the gravity terms are present for both phases (i.e., $\alpha = -1$, $\gamma = 0$, $\beta = 1/2$), obtaining

$$\frac{\partial \boldsymbol{u}_i^{(0)}}{\partial s} + \left(\boldsymbol{u}_i^{(0)} \cdot \nabla_y\right)\boldsymbol{u}_i^{(0)} = -\nabla_x p_i^{(0)} - \nabla_y p_i^{(1)} + \nabla_y^2 \boldsymbol{u}_i^{(0)} + \boldsymbol{e_g}, \quad \boldsymbol{x}, \boldsymbol{y} \in \mathcal{B}_i, \tag{C3}$$

where $i = 1, 2$. We multiply each term of equation (C3) with the velocity vector $\boldsymbol{u}_i^{(0)}$ and rearrange the nonlinear term in a divergence form (using the zero-order continuity equation $\nabla_y \cdot \boldsymbol{u}_i^{(0)} = 0$),

$$\frac{\partial}{\partial s}E_i^{(0)} + \nabla_y \cdot \left(\boldsymbol{u}_i^{(0)} E_i^{(0)}\right) = \boldsymbol{u}_i^{(0)} \cdot \left(-\nabla_x p_i^{(0)} + \boldsymbol{e}_g\right) - \boldsymbol{u}_i^{(0)} \cdot \nabla_y p_i^{(1)} + \boldsymbol{u}_i^{(0)} \cdot \left(\nabla_y \cdot \boldsymbol{\tau}_i^{(0)}\right), \tag{C4}$$

where $\boldsymbol{x}, \boldsymbol{y} \in \mathcal{B}_i$, while $\boldsymbol{\tau}_i^{(0)}$ and $E_i^{(0)} = 1/2 \left|\boldsymbol{u}_i^{(0)}\right|^2$ are the shear stress tensor and the kinetic energy based on $\boldsymbol{u}_i^{(0)}$, respectively. The flow is subject to the boundary conditions given by equations (B5a)–(B5d). Equation (C4) has the form of a (scalar) mechanical energy balance for the $\varepsilon^0$-order problem (i.e., a conservation law for the kinetic energy). Finally, we average equation (C4) over the unit cell $Y$ and the time period $T$.

By averaging of the unsteady term of equation (C4), we obtain an accumulation term $\mathcal{A}_i(\boldsymbol{x})$, which can be neglected only at steady state conditions, and it depends on the time derivative of the kinetic energy and the saturation only:

$$\mathcal{A}_i(\boldsymbol{x}) = \frac{1}{T|Y|}\int_T\int_{\mathcal{B}_i} \frac{\partial}{\partial s} E_i^{(0)} \mathrm{d}\boldsymbol{y}\mathrm{d}s = \left\langle \overline{\frac{\partial}{\partial s} E_i^{(0)}} \right\rangle. \tag{C5}$$

By averaging the nonlinear term of equation (C4) and using the divergence theorem, we obtain the Forchheimer term, $\mathcal{F}_i(\boldsymbol{x})$, which accounts for inertia effects over the unit cell and the time period:

$$\mathcal{F}_i(\boldsymbol{x}) = \frac{1}{T|Y|}\int_T\int_{\mathcal{B}_i} \nabla_y \cdot \left(\boldsymbol{u}_i^{(0)} E_i^{(0)}\right) \mathrm{d}\boldsymbol{y}\mathrm{d}s = \frac{1}{T|Y|}\int_T\int_{\Gamma} \boldsymbol{u}_i^{(0)} E_i^{(0)} \mathrm{d}\boldsymbol{y}\mathrm{d}s = \frac{\Gamma}{|Y|}\left\langle \overline{\boldsymbol{u}_i^{(0)} E_i^{(0)}} \right\rangle_\Gamma, \tag{C6}$$

where $\Gamma = \Gamma_i \cup \Gamma_{12} \cup \Gamma_{\text{in}} \cup \Gamma_{\text{out}}$ is the surface which bounds the volume $\mathcal{B}_i$ of the $i$th phase in the unit cell ($\Gamma_{\text{in}}$ and $\Gamma_{\text{out}}$ are the inflow and outflow surfaces). Note that such integral vanishes at the wall, on $\Gamma_1$ and $\Gamma_2$ (the flux is 0 at the wall due to the no-slip boundary condition). In this framework, $\mathcal{F}_i(\boldsymbol{x})$ can be modeled in terms of a kinetic energy flux across the bounding surfaces of each phase. In the limit of single phase flow, the modeling of the Forchheimer term is even simpler since we only need to know the kinetic energy flux at the inlet and at the outlet of the unit cell. In addition, $\mathcal{F}_i(\boldsymbol{x})$ vanishes for fully developed flow or sufficiently small $Re$ and $R \cdot Re$.

A further simplification of the Forchheimer term is obtained for the case of one-dimensional flow, where the dependence on the average velocity becomes explicit,

$$\mathcal{F}_i(\boldsymbol{x}) = \frac{1}{2}\phi S_i \mathcal{K}_i \omega_i \left\langle \overline{\boldsymbol{u}}_i \right\rangle_{\mathcal{B}_i}^3 \quad \text{with} \quad \omega_i = \frac{\left\langle \overline{\left(\boldsymbol{u}_i^{(0)}\right)^3} \right\rangle_\Gamma}{\left\langle \overline{\boldsymbol{u}}_i \right\rangle_{\mathcal{B}_i}^3}, \quad \mathcal{K}_i = \frac{|\Gamma|}{|\mathcal{B}_i|}, \tag{C7}$$

where $\omega_i$ is the shape factor which depends on the shape of the velocity profile on the bounding surfaces of each phase, while $\mathcal{K}_i$ is a function of the saturation only. The shape factor $\omega_i$ is the ratio of the local velocity elevated to power 3 and averaged on the bounding surfaces $\Gamma$, to the average velocity on the volume occupied by the $i$th phase elevated to the power 3. The definition of the shape factors is similar to the analogous shape factor coefficients commonly used in one-dimensional average modeling (see Picchi et al., 2014, 2017). Both these terms are fully determined once the phase topology (i.e., the pore-scale flow regime) and the velocity profiles are known (or assumed).

The average of the driving force terms yields

$$\frac{1}{T|Y|}\int_T\int_{\mathcal{B}_i} \boldsymbol{u}_i^{(0)} \cdot \left(-\nabla_x p_i^{(0)} + \boldsymbol{e}_g + \nabla_y p_i^{(1)}\right) \mathrm{d}\boldsymbol{y}\mathrm{d}s = -\nabla_x p_i \cdot \langle \overline{\boldsymbol{u}}_i \rangle + \mathcal{G}_i + \mathcal{P}_i(\boldsymbol{x}), \tag{C8}$$

where $p_i(\boldsymbol{x})$ is the macroscopic pressure, while the term $\mathcal{P}_i(\boldsymbol{x})$ includes the work done by the local pressure gradient: it is negligible for zero gradient in the geometry (e.g., a constant diameter capillary tube) and flat interface condition. $\mathcal{G}_i$ is the work done by the gravitational body force in the unit cell and over the time period defined as

$$\mathcal{G}_i = \frac{1}{T|Y|}\int_T\int_{\mathcal{B}_i} \boldsymbol{u}_i^{(0)} \cdot \boldsymbol{e}_g \mathrm{d}\boldsymbol{y}\mathrm{d}s. \tag{C9}$$

By averaging the viscous term in equation (C4), we obtain the work term, $\mathcal{W}_i(\boldsymbol{x})$, which includes the work done by the surface forces given by

$$\mathcal{W}_i(\boldsymbol{x}) = \frac{1}{T|Y|}\int_T\int_{\mathcal{B}_i} \boldsymbol{u}_i^{(0)} \cdot \left(\nabla_y \cdot \boldsymbol{\tau}_i^{(0)}\right) \mathrm{d}\boldsymbol{y}\mathrm{d}s. \tag{C10}$$

This term incorporates the interaction between flowing phases (shear-stress between phases at the fluid-fluid interface) and the solid (shear-stress t the solid wall) in the unit cell, and it strongly depends on the phase topology (i.e., the pore-scale flow regimes). Since we would like to easily incorporate such physics, we simplify $\mathcal{W}_i(\boldsymbol{x})$ such that its dependence on the average velocities, $\langle \overline{\boldsymbol{u}}_i \rangle_{\mathcal{B}_i}$, and the average shear stresses, $\langle \overline{\boldsymbol{\tau}}_i \rangle_{\mathcal{B}_i}$, becomes explicit, similarly to the approach described in Lahey and Drew (1988). Specifically, we can express $\mathcal{W}_i(\boldsymbol{x})$ as

$$\mathcal{W}_i(\boldsymbol{x}) = \left\langle \boldsymbol{u}_i^{(0)} \cdot \left( \nabla_y \cdot \boldsymbol{\tau}_i^{(0)} \right) \right\rangle = \phi S_i \left\langle \boldsymbol{u}_i^{(0)} \cdot \left( \nabla_y \cdot \boldsymbol{\tau}_i^{(0)} \right) \right\rangle_{\mathcal{B}_i}, \tag{C11}$$

and, for the one-dimensional flow,

$$\mathcal{W}_i(\boldsymbol{x}) = \phi S_i \langle \overline{\boldsymbol{u}}_i \rangle_{\mathcal{B}_i} \left[ \mathcal{T}_{f1} + \mathcal{T}_{wi} \right] + \dots, \tag{C12}$$

where

$$\mathcal{T}_{fi} = \langle \overline{\boldsymbol{\tau}}_f \rangle_{\mathcal{B}_i} \frac{\Gamma_{12}}{\mathcal{B}_i}, \quad \text{and} \quad \mathcal{T}_{wi} = \langle \overline{\boldsymbol{\tau}}_w \rangle_{\mathcal{B}_i} \frac{\Gamma_i}{\mathcal{B}_i}, \quad i = 1, 2, \tag{C13}$$

with $\mathcal{T}_{fi}$ and $\mathcal{T}_{wi}$ the interfacial and the wall stress term of the $i$th phase, respectively, $\Gamma_{12}$ the dimensionless fluid-fluid surface, $\Gamma_i$ the dimensionless fluid-wall interface of the $i$th phase, and $\mathcal{B}_i$ the dimensionless volume occupied by of the $i$th phase. $\langle \overline{\boldsymbol{\tau}}_f \rangle_{\mathcal{B}_i}$ and $\langle \overline{\boldsymbol{\tau}}_w \rangle_{\mathcal{B}_i}$ are the averaged dimensionless interfacial and wall shear stresses of the $i$th phase in the unit cell. This formulation of the shear stress terms has been inspired by the widely used closures in one-dimensional average models for pipe flow (Bertodano et al., 2017). Such closures are usually formulated in analogy with single-phase flow and only recently have been corrected to describe friction at the fluid-fluid interface and at the solid walls accurately (see Ullmann & Brauner, 2004; Ullmann et al., 2004). In this framework, modeling different flow regimes is straightforward: if the phase topology is known, one can both estimate the geometrical distribution of phases (i.e., the volume, the wetted surface, and the interfacial area as a function of the saturation) and construct the shear stress terms. For example, if the nonwetting phase is not in contact with the wall, the wall shear-stress term of the nonwetting phase is set zero, $\mathcal{T}_{wi} = 0$, while the interfacial one, $\mathcal{T}_{fi}$, should be properly modeled.

Finally, the homogenized equation of the $i$th phase has the following form:

$$\mathcal{A}_i + \mathcal{F}_i = -\nabla p_i \cdot \langle \overline{\boldsymbol{u}}_i \rangle - \mathcal{P}_i + \mathcal{W}_i + \mathcal{G}_i \qquad \boldsymbol{x} \in \Omega. \tag{C14}$$

A general discussion on the effect of the order of magnitude of the Reynolds number, the density and viscosity ratio is provided in section 3.2. In addition, since all the terms in equation (C14) have been defined, we proceed by, first, postulating the phase topology at the pore-scale, and then, deriving regime-specific upscaled equations in section 4.

**Acknowledgments**
Full support by the Department of Energy under the Early Career award DE-SC0014227 *Multiscale dynamics of reactive fronts in the subsurface* is gratefully acknowledged. The paper is theoretical, and no data are used.

## References

Abu-Al-Saud, M. O., Riaz, A., & Tchelepi, H. A. (2017). Multiscale level-set method for accurate modeling of immiscible two-phase flow with deposited thin films on solid surfaces. *Journal of Computational Physics*, *333*, 297–320. http://doi.org/10.1016/j.jcp.2016.12.038

Alexander, F. J., Garcia, A. L., & Tartakovsky, D. M. (2005). Noise in algorithm refinement methods. *Computing in Science & Engineering*, *7*(3), 32–38.

Amir, K., Xiongyu, C., & DiCarlo, D. A. (2015). The effect of saturation path on three-phase relative permeability. *Water Resources Research*, *51*, 9141–9164. https://doi.org/10.1002/2015WR017185

Armstrong, R. T., McClure, J. E., Berrill, M. A., Rücker, M., Schlüter, S., & Berg, S. (2016). Beyond Darcy's law: The role of phase topology and ganglion dynamics for two-fluid flow. *Physical Review E*, *94*, 43113. https://doi.org/10.1103/PhysRevE.94.043113

Armstrong, R. T., McClure, J. E., Berrill, M. A., Rücker, M., Schlüter, S., & Berg, S. (2017). Flow regimes during immiscible displacement. *Petrophysics*, *58*, 10–18.

Armstrong, R. T., Ott, H., Georgiadis, A., Rucker, M., Schwing, A., & Berg, S. (2014). Subsecond pore-scale displacement processes and relaxation dynamics in multiphase flow. *Water Resources Research*, *50*, 9162–9176. https://doi.org/10.1002/2014WR015858

Armstrong, R. T., Porter, M. L., & Wildenschild, D. (2012). Linking pore-scale interfacial curvature to column-scale capillary pressure. *Advances in Water Resources*, *46*, 55–62. https://doi.org/10.1016/j.advwatres.2012.05.009

Arunachalam, H., Onori, S., & Battiato, I. (2015). On veracity of macroscopic lithium-ion battery models. *Journal of the Electrochemical Society*, *162*(10), A1940–A1951. https://doi.org/10.1149/2.0771509jes

Auriault, J. L. (1987). Nonsaturated deformable porous media: Quasistatics. *Transport in Porous Media*, *2*(1), 45–64. https://doi.org/10.1007/BF00208536

Auriault, J. L., & Adler, P. M. (1995). Taylor dispersion in porous media: Analysis by multiple scale expansions. *Advances in Water Resources*, *18*(4), 217–226. https://doi.org/10.1016/0309-1708(95)00011-7

Auriault, J. L., Lebaigue, O., & Bonnet, G. (1989). Dynamics of two immiscible fluids flowing through deformable porous media. *Transport in Porous Media*, *4*(2), 105–128. https://doi.org/10.1007/BF00134993

Avraam, D. G., & Payatakes, A. C. (1995a). Flow regimes and relative permeabilities during steady-state two-phase flow in porous media. *Journal of Fluid Mechanics*, *293*, 207–236. https://doi.org/10.1017/S0022112095001698

Avraam, D. G., & Payatakes, A. C. (1995b). Generalized relative permeability coefficients during steady-state two-phase flow in porous media, and correlation with the flow mechanisms. *Transport in Porous Media*, *20*(1), 135–168. https://doi.org/10.1007/BF00616928

Ayub, M., & Bentsen, R. G. (1999). Interfacial viscous coupling: A myth or reality? *Journal of Petroleum Science and Engineering*, *23*(1), 13–26. https://doi.org/10.1016/S0920-4105(99)00003-0

Battiato, I., & Tartakovsky, D. M. (2011). Applicability regimes for macroscopic models of reactive transport in porous media. *Journal of Contaminant Hydrology*, *120-121*(C), 18–26. https://doi.org/10.1016/j.jconhyd.2010.05.005

Battiato, I., Tartakovsky, D. M., Tartakovsky, A. M., & Scheibe, T. D. (2011). Hybrid models of reactive transport in porous and fractured media. *Advances in Water Resources*, *34*(9), 1140–1150.

Bear, J. (1972). *Dynamics of Fluids in Porous Media*, Dover Civil and Mechanical Engineering Series. New York: American Elsevier Publishing Company.

Bear, J., & Cheng, A. (2016). *Modeling Groundwater Flow and Contaminant Transport*. New York: Springer Netherlands.

Berg, S., Cense, A. W., Hofman, J. P., & Smits, R. M. M. (2008). Two-phase flow in porous media with slip boundary condition. *Transport in Porous Media*, *74*(3), 275–292. https://doi.org/10.1007/s11242-007-9194-4

Bertodano, M. L., Fullmer, W., Clausse, A., & Ransom, V. (2017). *Two-Fluid Model Stability, Simulation and Chaos*. Cham, Switzerland: Springer International Publishing.

Blunt, M. (2017). *Multiphase Flow in Permeable Media: A Pore-Scale Perspective*. Cambridge, UK: Cambridge University Press.

Blunt, M. J., Bijeljic, B., Dong, H., Gharbi, O., Iglauer, S., Mostaghimi, P., et al. (2013). Pore-scale imaging and modelling. *Advances in Water Resources*, *51*, 197–216.

Boso, F., & Battiato, I. (2013). Homogenizability conditions for multicomponent reactive transport. *Advances in Water Resources*, *62*, 254–265. https://doi.org/10.1016/j.advwatres.2013.07.014

Brauner, N. (1990). On the relations between two-phase flows under reduced gravity and Earth experiment. *International Communications in Heat and Mass Transfer*, *17*(3), 271–281. https://doi.org/10.1016/0735-1933(90)90092-X

Bretherton, F. P. (1961). The motion of long bubbles in tubes. *Journal of Fluid Mechanics*, *10*(2), 166–188. https://doi.org/10.1017/S0022112061000160.

Cazarez, O., Montoya, D., Vital, A., & Bannwart, A. (2010). Modeling of three-phase heavy oil–water–gas bubbly flow in upward vertical pipes. *International Journal of Multiphase Flow*, *36*(6), 439–448. https://doi.org/10.1016/j.ijmultiphaseflow.2010.01.006

Chen, X., & DiCarlo, D. A. (2016). A new unsteady-state method of determining two-phase relative permeability illustrated by $CO_2$-brine primary drainage in berea sandstone. *Advances in Water Resources*, *96*, 251–265. https://doi.org/10.1016/j.advwatres.2016.07.018

Chen, X., Gao, S., Kianinejad, A., & DiCarlo, D. A. (2017). *Water Resources Research*, *53*, 6312–6321. https://doi.org/10.1002/2017WR020810

Chen, Z., Lyons, S. L., & Qin, Guan (2001). Derivation of the Forchheimer law via homogenization. *Transport in Porous Media*, *44*(2), 325–335. https://doi.org/10.1023/A:1010749114251

Cinar, Y., & Riaz, A. (2014). Carbon dioxide sequestration in saline formations: Part 2—Review of multiphase flow modeling. *Journal of Petroleum Science and Engineering*, *124*, 381–398. https://doi.org/10.1016/j.petrol.2014.07.023

Daly, K. R., & Roose, T. (2015). Homogenization of two fluid flow in porous media. *Proceedings of the Royal Society of London A: Mathematical, Physical and Engineering Sciences*, *471*(2176), 20140564. https://doi.org/10.1098/rspa.2014.0564

Darcy, H. (1856). Détermination Des Lois d'écoulement de l'eau á travers le sable.

Datta, S. S., Dupin, J.-B., & Weitz, D. A. (2014). Fluid breakup during simultaneous two-phase flow through a three-dimensional porous medium. *Physics of Fluids*, *26*(6), 62004. https://doi.org/10.1063/1.4884955

Fabre, J., & Line, A. (1992). Modeling of two-phase slug flow. *Annual Review of Fluid Mechanics*, *24*(1), 21–46. https://doi.org/10.1146/annurev.fl.24.010192.000321

Forchheimer, P. (1901). Wasserbewegung durch boden. *Wasserbewegung Durch Boden*, *49*, 1782–1788.

Gao, Y., Lin, Q., Bijeljic, B., & Blunt, M. J. (2017). X-ray microtomography of intermittency in multiphase flow at steady state using a differential imaging method. *Water Resources Research*, *53*(12), 10,274–10,292. https://doi.org/10.1002/2017WR021736

Garing, C., de Chalendar, J. A., Voltolini, M., Ajo-Franklin, J. B., & Benson, S. M. (2017). Pore-scale capillary pressure analysis using multi-scale X-ray micromotography. *Advances in Water Resources*, *104*, 223–241. https://doi.org/10.1016/j.advwatres.2017.04.006

Gray, W. G., Dye, A. L., McClure, J. E., Pyrak-Nolte, L. J., & Miller, C. T. (2015). On the dynamics and kinematics of two-fluid-phase flow in porous media. *Water Resources Research*, *51*, 5365–5381. https://doi.org/10.1002/2015WR016921

Gray, W. G., & Miller, C. T. (2010). Thermodynamically constrained averaging theory approach for modeling flow and transport phenomena in porous medium systems: 8. Interface and common curve dynamics. *Advances in Water Resources*, *33*(12), 1427–1443. https://doi.org/10.1016/j.advwatres.2010.07.002

Hassanizadeh, M., & Gray, W. G. (1980). General conservation equations for multi-phase systems: 3. Constitutive theory for porous media flow. *Advances in Water Resources*, *3*(1), 25–40. https://doi.org/10.1016/0309-1708(80)90016-0

Hassanizadeh, S., & Gray, W. G. (1990). Mechanics and thermodynamics of multiphase flow in porous media including interphase boundaries. *Advances in Water Resources*, *13*(4), 169–186. https://doi.org/10.1016/0309-1708(90)90040-B

Hassanizadeh, S. M., & Gray, W. G. (1993a). Thermodynamic basis of capillary pressure in porous media. *Water Resources Research*, *29*(10), 3389–3405. https://doi.org/10.1029/93WR01495

Hassanizadeh, S. M., & Gray, W. G. (1993b). Toward an improved description of the physics of two-phase flow. *Advances in Water Resources*, *16*(1), 53–67. https://doi.org/10.1016/0309-1708(93)90029-F

Hilfer, R. (1998). Macroscopic equations of motion for two-phase flow in porous media. *Physical Review E*, *58*, 2090–2096. https://doi.org/:10.1103/PhysRevE.58.2090

Hilfer, R. (2006). Macroscopic capillarity and hysteresis for flow in porous media. *Physical Review E*, *73*, 16307. https://doi.org/10.1103/PhysRevE.73.016307

Hodges, S. R., Jensen, O. E., & Rallison, J. M. (2004). The motion of a viscous drop through a cylindrical tube. *Journal of Fluid Mechanics*, *501*, 279–301. https://doi.org/10.1017/S0022112003007213

Hornung, U. (Ed.) (1997). *Homogenization and Porous Media Edited by* Hornung, U. New York, NY, USA: Springer-Verlag New York, Inc.

Hout, R. V., Shemer, L., & Barnea, D. (1992). Spatial distribution of void fraction within a liquid slug and some other related slug parameters. *International Journal of Multiphase Flow*, *18*(6), 831–845. https://doi.org/10.1016/0301-9322(92)90062-L

Jackson, A. S., Miller, C. T., & Gray, W. G. (2009). Thermodynamically constrained averaging theory approach for modeling flow and transport phenomena in porous medium systems: 6. Two-fluid-phase flow. *Advances in Water Resources*, *32*(6), 779–795. https://doi.org/10.1016/j.advwatres.2008.11.010

Jovanovic, J., Zhou, W., Rebrov, E. V., Nijhuis, T. A., Hessel, V., & Schouten, J. C. (2011). Liquid-liquid slug flow: Hydrodynamics and pressure drop. *Chemical Engineering Science*, *66*(1), 42–54. https://doi.org/10.1016/j.ces.2010.09.040
Kalaydjian, F. (1987). A macroscopic description of multiphase flow in porous media involving spacetime evolution of fluid/fluid interface. *Transport in Porous Media*, *2*(6), 537–552. https://doi.org/10.1007/BF00192154
Karadimitriou, N. K., Hassanizadeh, S. M., Joekar-Niasar, V., & Kleingeld, P. J. (2014). Micromodel study of two-phase flow under transient conditions: Quantifying effects of specific interfacial area. *Water Resources Research*, *50*, 8125–8140. https://doi.org/10.1002/2014WR015388
Kashid, M. N., & Agar, D. W. (2007). Hydrodynamics of liquid–liquid slug flow capillary microreactor: Flow regimes, slug size and pressure drop. *Chemical Engineering Journal*, *131*(1), 1–13. https://doi.org/10.1016/j.cej.2006.11.020
Kawahara, A., Chung, P.-Y., & Kawaji, M. (2002). Investigation of two-phase flow pattern, void fraction and pressure drop in a microchannel. *International Journal of Multiphase Flow*, *28*(9), 1411–1435. https://doi.org/10.1016/S0301-9322(02)00037-X
Kianinejad, A., Chen, X., & DiCarlo, D. A. (2016). Direct measurement of relative permeability in rocks from unsteady-state saturation profiles. *Advances in Water Resources*, *94*, 1–10. https://doi.org/10.1016/j.advwatres.2016.04.018
Korneev, S., & Battiato, I. (2016). Sequential homogenization of reactive transport in polydisperse porous media. *Multiscale Modeling & Simulation*, *14*(4), 1301–1318. https://doi.org/10.1137/16M1074278
Lahey, R. T., & Drew, D. A. (1988). *The Three-Dimensional Time and Volume Averaged Conservation Equations of Two-Phase Flow* (pp. 1–69). Boston, MA: Springer US.
Lake, L. W. (1989). *Enhanced Oil Recovery*. Englewood Cliffs, NJ: Prentice Hall.
Lasseux, D., Ahmadi, A., & Arani, A. A. A. (2008). Two-phase inertial flow in homogeneous porous media: A theoretical derivation of a macroscopic model. *Transport in Porous Media*, *75*(3), 371–400. https://doi.org/10.1007/s11242-008-9231-y
Lenormand, R., Zarcone, C., & Sarr, A. (1983). Mechanisms of the displacement of one fluid by another in a network of capillary ducts. *Journal of Fluid Mechanics*, *135*, 337–353. https://doi.org/10.1017/S0022112083003110
Leverett, M. C. (1941). Capillary behavior in porous solids. *Society of Petroleum Engineers*, *142*, 152–169.
Ling, B., Bao, J., Oostrom, M., Battiato, I., & Tartakovsky, A. M. (2017). Modeling variability in porescale multiphase flow experiments. *Advances in Water Resources*, *105*, 29–38.
Løvoll, G., Jankov, M., Måløy, K. J., Toussaint, R., Schmittbuhl, J., Schäfer, G., & Méheust, Y. (2011). Influence of viscous fingering on dynamic saturation–pressure curves in porous media. *Transport in Porous Media*, *86*(1), 305–324. https://doi.org/10.1007/s11242-010-9622-8
Marle, C. M. (1982). On macroscopic equations governing multiphase flow with diffusion and chemical reactions in porous media. *International Journal of Engineering Science*, *20*(5), 643–662. https://doi.org/10.1016/0020-7225(82)90118-5
Marusic-Paloka, E., & Mikelic, A. (2000). The derivation of a nonlinear filtration law including the inertia effects via homogenization. *Nonlinear Analysis: Theory, Methods & Applications*, *42*(1), 97–137. https://doi.org/10.1016/S0362-546X(98)00346-0
McClure, J. E., Armstrong, R. T., Berrill, M. A., Schlüter, S., Berg, S., Gray, W. G., & Miller, C. T. (2018). A geometric state function for two-fluid flow in porous media. Physical Review Fluids, in press(https://arxiv.org/pdf/1805.11032.pdf).
McClure, J. E., Berrill, M. A., Gray, W. G., & Miller, C. T. (2016a). Tracking interface and common curve dynamics for two-fluid flow in porous media. *Journal of Fluid Mechanics*, *796*, 211–232. https://doi.org/10.1017/jfm.2016.212
McClure, J. E., Berrill, M. A., Gray, W. G., & Miller, C. T. (2016b). Influence of phase connectivity on the relationship among capillary pressure, fluid saturation, and interfacial area in two-fluid-phase porous medium systems. *Physical Review E*, *94*, 33102. https://doi.org/10.1103/PhysRevE.94.033102
Mei, C. C., & Auriault, J. L. (1991). The effect of weak inertia on flow through a porous medium. *Journal of Fluid Mechanics*, *222*, 647–663. https://doi.org/10.1017/S0022112091001258
Moghadasi, L., Guadagnini, A., Inzoli, F., Bartosek, M., & Renna, D. (2016). Characterization of two- and three-phase relative permeability of water-wet porous media through X-ray saturation measurements. *Journal of Petroleum Science and Engineering*, *145*, 453–463. https://doi.org/10.1016/j.petrol.2016.05.031
Niessner, J., Berg, S., & Hassanizadeh, S. M. (2011). Comparison of two-phase Darcy's law with a thermodynamically consistent approach. *Transport in Porous Media*, *88*(1), 133–148. https://doi.org/10.1007/s11242-011-9730-0
Niessner, J., & Hassanizadeh, S. M. (2008). A model for two-phase flow in porous media including fluid-fluid interfacial area. *Water Resources Research*, *44*(8), W08439. http://doi.org/10.1029/2007WR006721
Nordbotten, J. M., Celia, M. A., Dahle, H. K., & Hassanizadeh, S. M. (2007). Interpretation of macroscale variables in Darcy's law. *Water Resources Research*, *43*, W08430. http://doi.org/10.1029/2006WR005018
Nordbotten, J. M., Celia, M. A., Dahle, H. K., & Hassanizadeh, S. M. (2008). On the definition of macroscale pressure for multiphase flow in porous media. *Water Resources Research*, *44*(6), W06S02. https://doi.org/10.1029/2006WR005715
Picchi, D., Correra, S., & Poesio, P. (2014). Flow pattern transition, pressure gradient, hold-up predictions in gas/non-Newtonian power-law fluid stratified flow. *International Journal of Multiphase Flow*, *63*, 105–115. https://doi.org/10.1016/j.ijmultiphaseflow.2014.03.005
Picchi, D., Manerba, Y., Correra, S., Margarone, M., & Poesio, P. (2015b). Gas/shear-thinning liquid flows through pipes: Modeling and experiments. *International Journal of Multiphase Flow*, *73*, 217–226. https://doi.org/10.1016/j.ijmultiphaseflow.2015.03.005
Picchi, D., Poesio, P., Ullmann, A., & Brauner, N. (2017). Characteristics of stratified flows of Newtonian/non-Newtonian shear-thinning fluids. *International Journal of Multiphase Flow*, *97*, 109–133. urlhttps://doi.org/10.1016/j.ijmultiphaseflow.2017.06.005.
Picchi, D., Strazza, D., Demori, M., Ferrari, V., & Poesio, P. (2015a). An experimental investigation and two-fluid model validation for dilute viscous oil in water dispersed pipe flow. *Experimental Thermal and Fluid Science*, *60*, 28–34. https://doi.org/10.1016/j.expthermflusci.2014.07.016
Picchi, D., Ullmann, A., & Brauner, N. (2018). Modeling of core-annular and plug flows of Newtonian/non-Newtonian shear-thinning fluids in pipes and capillary tubes. *International Journal of Multiphase Flow*, *103*, 43–60. https://doi.org/10.1016/j.ijmultiphaseflow.2018.01.023
Prodanovic, M., Esteva, M., Hanlon, M., Nanda, G., & Agarwal, P. (2015). Digital rocks portal: A repository for porous media images.
Prodanovic, M., Lindquist, W. B., & Seright, R. S. (2007). 3D image-based characterization of fluid displacement in a Berea core. *Advances in Water Resources*, *30*, 214–226.
Reynolds, C. A., Menke, H., Andrew, M., Blunt, M. J., & Krevor, S. (2017). Dynamic fluid connectivity during steady-state multiphase flow in a sandstone. *Proceedings of the National Academy of Sciences*, *114*(31), 8187–8192. https://doi.org/10.1073/pnas.1702834114
Roumpea, E., Chinaud, M., & Angeli, P. (2017). Experimental investigations of non-Newtonian/Newtonian liquid-liquid flows in microchannels. *AIChE Journal*, *63*(8), 3599–3609. https://doi.org/10.1002/aic.15704
Rucker, M., Berg, S., Armstrong, R. T., Georgiadis, A., Ott, H., Schwing, A., et al. (2015). From connected pathway flow to ganglion dynamics. *Geophysical Research Letters*, *42*, 3888–3894. https://doi.org/10.1002/2015GL064007
Rybak, I., Gray, W., & Miller, C. (2015). Modeling two-fluid-phase flow and species transport in porous media. *Journal of Hydrology*, *521*, 565–581. https://doi.org/10.1016/j.jhydrol.2014.11.051
Sanchez-Palencia, E. (1980). *Homogeneous Media and Vibration Theory*. New York: Springer-Verlag Berlin Heidelberg.

Singh, K., Bijeljic, B., & Blunt, M. J. (2016). Imaging of oil layers, curvature and contact angle in a mixed-wet and a water-wet carbonate rock. *Water Resources Research*, *52*, 1716–1728. https://doi.org/10.1002/2015WR018072

Slattery, J. C. (1968). Multiphase viscoelastic flow through porous media. *AIChE Journal*, *14*(1), 50–56. https://doi.org/10.1002/aic.690140112

Slattery, J. C. (1970). Two-phase flow through porous media. *AIChE Journal*, *16*(3), 345–352. https://doi.org/10.1002/aic.690160306

Tartakovsky, A. M., & Meakin, P. (2006). Pore scale modeling of immiscible and miscible fluid flows using smoothed particle hydrodynamics. *Advances in Water Resources*, *29*(10), 1464–1478. https://doi.org/10.1016/j.advwatres.2005.11.014

Tomin, P., & Lunati, I. (2013). Hybrid multiscale finite volume method for two-phase flow in porous media. *Journal of Computational Physics*, *250*, 293–307.

Tsaoulidis, D., & Angeli, P. (2016). Effect of channel size on liquid-liquid plug flow in small channels. *AIChE Journal*, *62*(1), 315–324. https://doi.org/10.1002/aic.15026

Ullmann, A., & Brauner, N. (2004). Closure relations for the shear stresses in two-fluid models for core-annular flow. *Multiphase Science and Technology*, *16*(4), 355–387.

Ullmann, A., & Brauner, N. (2007). The prediction of flow pattern maps in minichannel. *Multiphase Science and Technology*, *19*(1), 49–73.

Ullmann, A., Goldstein, A., Zamir, M., & Brauner, N. (2004). Closure relations for the shear stresses in two-fluid models for laminar stratified flow. *International Journal of Multiphase Flow*, *30*(7), 877–900. https://doi.org/10.1016/j.ijmultiphaseflow.2004.03.008

Wegmann, A., & von Rohr, P. R. (2006). Two phase liquid-liquid flows in pipes of small diameters. *International Journal of Multiphase Flow*, *32*(8), 1017–1028. https://doi.org/10.1016/j.ijmultiphaseflow.2006.04.001

Whitaker, S. (1986). Flow in porous media II: The governing equations for immiscible, two-phase flow. *Transport in Porous Media*, *1*(2), 105–125. https://doi.org./10.1007/BF00714688

Wyckoff, R. D., & Botset, H. G. (1936). The flow of gas-liquid mixtures through unconsolidated sands. *Physics*, *7*(9), 325–345. https://doi.org/10.1063/1.1745402

Xu, X., & Wang, X. (2014). Non-Darcy behavior of two-phase channel flow. *Physical Review E*, *90*, 23010. htttps://doi.org/10.1103/PhysRevE.90.023010

Yagodnitsyna, A. A., Kovalev, A. V., & Bilsky, A. V. (2016). Flow patterns of immiscible liquid-liquid flow in a rectangular microchannel with T-junction. *Chemical Engineering Journal*, *303*, 547–554. https://doi.org/10.1016/j.cej.2016.06.023

Yang, H., Xu, Z., Fan, M., Gupta, R., Slimane, R. B, Bland, A. E, & Wright, I. (2008). Progress in carbon dioxide separation and capture: A review. *Journal of Environmental Sciences*, *20*(1), 14–27. https://doi.org/10.1016/S1001-0742(08)60002-9

Yousefzadeh, M., & Battiato, I. (2017). Physics-based hybrid method for multiscale transport in porous media. *Journal of Computational Physics*, *344*, 320–338.